AD-E300 218

FOR FURTHER TRAN

AD A055931

(6)

(18) SBIE (19) AD-E300 218

DNA 4470F

THERMAL LAYER DEVELOPMENT MODELING

Science Applications, Inc.
8400 Westpark Drive
McLean, Virginia 22101

(10) T. M. Knasel
P. L. Versteegen
J. A. Powers

(12)

(12) 118 p.

(11) June 1977

(9) Final Report for Period 1 December 1975 – 20 June 1977.

(14) SAI-78-541-WA

CONTRACT No. DNA 001-76-C-0176 (15)

AD No.
DDC FILE COPY

APPROVED FOR PUBLIC RELEASE;
DISTRIBUTION UNLIMITED.

62704H

THIS WORK SPONSORED BY THE DEFENSE NUCLEAR AGENCY
UNDER RDT&E RMSS CODE B344076464 X99QAXSA00186 H2590D.

(16)

(17) A001

DDC
RECEIVED
JUL 5 1978
B

Prepared for

Director
DEFENSE NUCLEAR AGENCY
Washington, D. C. 20305

408 404

REPORT DOCUMENTATION PAGE

READ INSTRUCTIONS BEFORE COMPLETING FORM

1. REPORT NUMBER DNA 4470F

2. GOVT ACCESSION NO.

3. RECIPIENT'S CATALOG NUMBER

4. TITLE (and Subtitle) THERMAL LAYER DEVELOPMENT MODELING

5. TYPE OF REPORT & PERIOD COVERED
Final Report for Period
1 Dec 75—20 Jun 77

6. PERFORMING ORG. REPORT NUMBER SAI-78-541-WA

7. AUTHOR(s)
T. M. Knasel
P. L. Versteegen
J. A. Powers

8. CONTRACT OR GRANT NUMBER(s) DNA 001-76-C-0176 new

9. PERFORMING ORGANIZATION NAME AND ADDRESS
Science Applications, Inc.
8400 Westpark Drive
McLean, Virginia 22101

10. PROGRAM ELEMENT, PROJECT, TASK AREA & WORK UNIT NUMBERS NWED Subtask X99QAXSA001-86

11. CONTROLLING OFFICE NAME AND ADDRESS
Director
Defense Nuclear Agency
Washington, D.C. 20305

12. REPORT DATE June 1977

13. NUMBER OF PAGES 122

14. MONITORING AGENCY NAME & ADDRESS (if different from Controlling Office)

15. SECURITY CLASS (of this report) UNCLASSIFIED

15a. DECLASSIFICATION/DOWNGRADING SCHEDULE

16. DISTRIBUTION STATEMENT (of this Report)

Approved for public release; distribution unlimited.

17. DISTRIBUTION STATEMENT (of the abstract entered in Block 20, if different from Report)

18. SUPPLEMENTARY NOTES

This work sponsored by the Defense Nuclear Agency under RDT&E RMSS Code B344076464 X99QAXSA00186 H2590D.

19. KEY WORDS (Continue on reverse side if necessary and identify by block number)

Thermal Layer
Nuclear Weapon Thermal Effects
Soil Blowoff

20. ABSTRACT (Continue on reverse side if necessary and identify by block number)

Thermal layers which may develop during the employment of nuclear weapons have been investigated theoretically. If such a layer forms, non-ideal shock wave propagation results. This in turn modifies the potential damage levels, adding risk and uncertainty to the sure-kill and sure-safe areas around the burst point. In this study ~~the authors~~ calculate the effective thermal layer temperature for a series of atmospheric nuclear explosions conducted at the Nevada Test Site. By reinterpretation of previous evidence, good agreement between layer temperature and shock propagation behavior is evident. From

next page

20. ABSTRACT (Continued)

additional data on soil response to strong thermal radiation, ~~the authors were able to construct~~ a semi-empirical model of thermal layer temperature distributions and dust generation was constructed based on first principles. This model agrees with the known values of thermal layer parameters including those of layer temperature.

PREFACE

The authors wish to thank the following for important scientific contributions and assistance in these efforts: Dr. R. T. Liner, Jr., Dr. John E. Mansfield and Mr. Frank Varcolik. The assistance of the Defense Nuclear Agency, in particular Capt. Jerry Stockton of SPSS, the contract technical monitor, is appreciated.

TABLE OF CONTENTS

TABLE OF CONTENTS (Cont'd)

TABLE OF CONTENTS (Cont'd)

LIST OF ILLUSTRATIONS

LIST OF ILLUSTRATIONS (Cont'd)

LIST OF TABLES

Section 1

INTRODUCTION

1.1 PURPOSE AND SCOPE

Efficient military planning of both a tactical and strategic nature requires a certain degree of accuracy in the predictions of nuclear weapons effects. The optimum accuracy depends on the scenarios under consideration. In many instances the predictions of weapon effects may be uncertain because of lack of actual test data for use in calibrating and verifying the appropriate weapons effects models. A case in point involves the propagation of nuclear air blast waves over surfaces previously heated by thermal radiation. The presence of a hot air layer just above the surface, a thermal layer, causes blast wave distortion, the precursor effect.[1,2] Surfaces that respond to the weapon thermal output and cause thermal layers to develop are classified as non-ideal in contrast to ideal surfaces over which no hot layer is formed.[3,4] A brief summary of some of the variation in weapon effectiveness caused by surfaces effects is shown in Table 1. Changes in ground range for effects reflect themselves in biased probabilities of target damage and the potential for sub-optimal allocation of weapons. In some cases studied the upper range of weapons required is 200% of the nominal number due to uncertainty in surface response in target area.[3]

Detailed knowledge (and reduced uncertainty) of the air blast effects can be obtained from calculations that require as input a model of the development of the thermal layer. The purpose of this report is to document a 1-year program conducted by Science Applications, Inc. (SAI), under the sponsorship of the Defense Nuclear Agency (DNA) directed toward that goal. The object of the work was to obtain a model of thermal layer development that uses experimental insight, is based on physical principles, and can be extended to study a wide range of surface parameters. The programmatic goals and milestones of this development, including earlier SAI work under

Table 1. COMPARISON OF IDEAL VERSUS NON-IDEAL AIR BLAST EFFECTS

- Reduced ground range, R, to obtain a given static pressure. For example, $\Delta R/R \sim 50\%$ at 15 psi for a scaled height of burst of 200 to 800 $\mathrm{ft/KT}^{1/3}$

- HOB for maximum static pressure near zero for non-ideal surface, for static pressures of 20 to 200 psi (according to EM-1)

- Increased dynamic pressure, $\Delta R/R = 50\%$, 150 to 15 psi for non-ideal case

- Increased dust loading of air — by orders of magnitude, pre-shock compared to ideal

- All non-ideal effects are strong functions of yield HOB and surface conditions (such as moisture).

Sources: References 3, 4 and 5.

previous DNA contracts, are shown in Table 2. The first stage in this work was the identification of basic physical mechanisms, then a model was developed for dry dusty soils (such as those found at the Nevada Test Site, NTS), and the final stage involved data analysis of solar furnace irradiation tests of a variety of soil types. These test results suggested the final form of a model that could include a wide variety of surfaces. Thus the model, while based on physical principles, uses test data wherever possible to account for processes inherently difficult to model in detail. Reports on previous segments of this work, as well as more detailed background information about the model development, are found in References 1 and 2.

1.2 THE PHYSICAL DEVELOPMENT OF A THERMAL LAYER

Thermal radiation from a nuclear explosion passes through air relatively unattenuated and upon striking a surface begins a rapid heating process. Due to the enormous energy release, this heating is extremely rapid, causing drastic imbalances in the surface structures which lead to the phenomenon of thermal blowoff. Such physical and chemical reactions as boiling of free water, evolution of bound water, and CO_2 or uneven thermal expansion of grains may be responsible for the effects observed. The air above the surface is heated in two ways: by direct contact with the surface, i.e., conduction, and later by convection. Also, the particles of blown-off material absorb thermal radiation and continue to heat. This heat is conducted to the air as the particles flow through the layer. Some of the processes that take place are shown in Figure 1. The thermal layer development is one of unstable equilibrium, and complex feedback mechanisms are probably at work. For instance, the blown-off dust shields the surface, suppressing further blowoff. Moreover, many of the detailed processes are inherently difficult to model; the amount of material blowoff is an example. A first principles thermo and hydrodynamic model is therefore nearly impossible to

Table 2. THERMAL LAYER MODEL DEVELOPMENT

Goals	Milestones
• Understand the basic mechanisms of thermal layer formation (previous contract)	• Identification of the role of dust blowoff due to thermal pulse causing volumetric air heating, and ground shielding; 6/73. • Basic model for dry, dusty soils (e.g., NTS) formulated; 6/74.
• Quantify the response of NTS type soils (previous contract)	• Coupling of experimental values for dust generation into model. Prediction of thermal layer development in agreement with temperatures "backed out" of NTS test data; 3/75. • First version for NTS soils completed; 6/75.
• Develop a model for the thermal layer (present contract)	• Identification of role of conduction in early time thermal layer formation. Agreement with solar furnace experiments obtained; 9/75. • Prediction of single particle trajectories as measured in WSMR tests; 4/76. • "Flux tube" approach developed to couple dust interactively to flow; 6/76. • Conduction, particle interaction coupled together. Model tested and verified; 9/76. • Parametric studies of model sensitivity; 10/76.

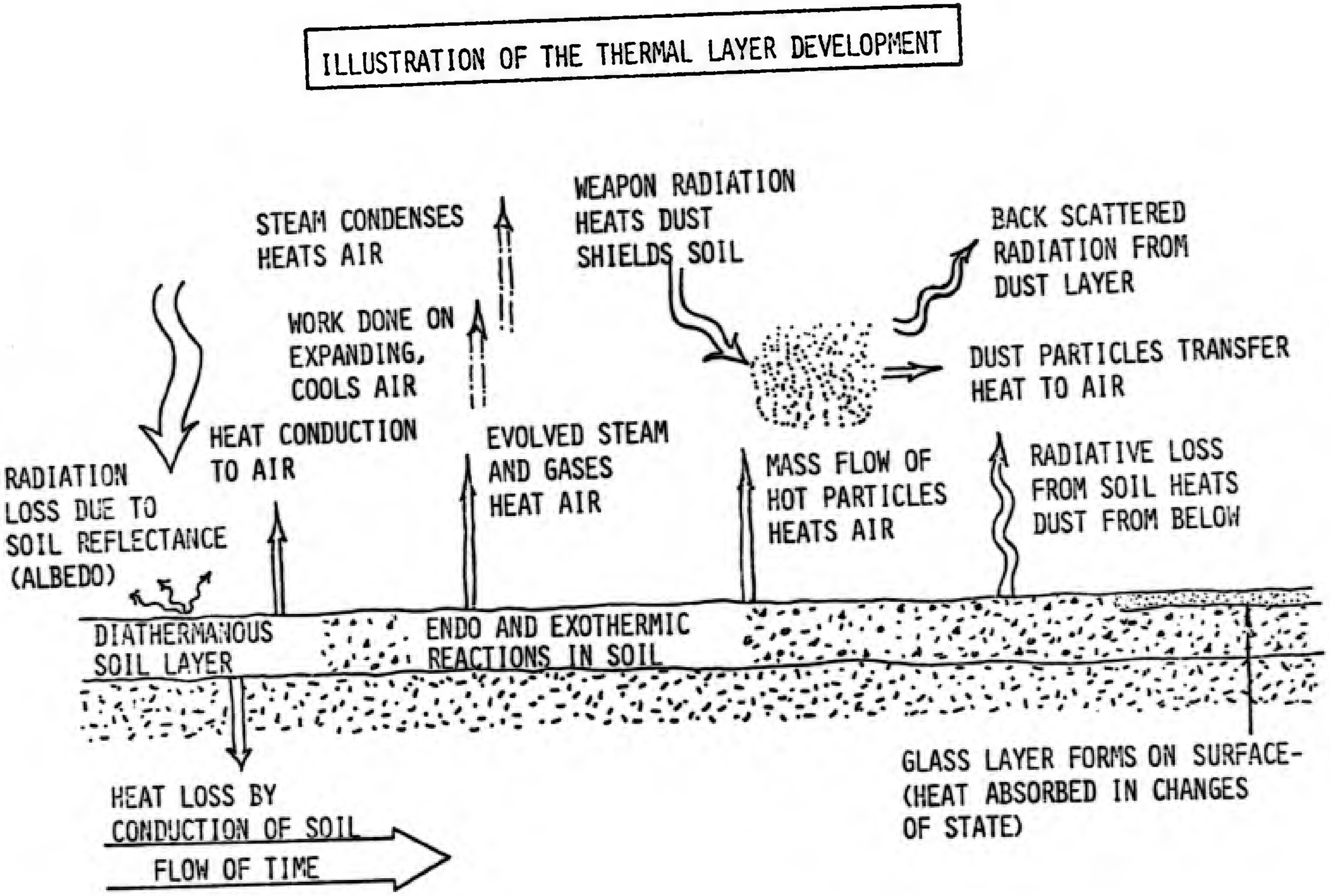

Figure 1. Illustration of the Response of a Non-Ideal Surface — The Thermal Layer Development Results from Rapid Radiant Heating

construct. A successful model can rely on experimental data for many parts of the problem. The model SAI has developed accounts for the complexity and instability of the development, inputting test data on the amount and distribution of blown-off material. A more inclusive report on thermal layer development is found in Reference 3.

1.3 DEFINITION OF NON-IDEAL SURFACE

A surface that results in the development of a thermal layer is classified as thermally non-ideal. In contrast, a surface that lacks the chemical and physical properties to initiate blowoff and is heat reflecting so as to suppress conduction as well is thermally ideal. An aluminum plate is an example of the latter. The authoritative compendium of surface classification is found in two references, EM-1 and DASA 1200 (References 4 and 5), where surfaces are divided into two classes, near ideal and non-ideal. This classification information is summarized in Table 3, which also includes comments based on present knowledge of surface response. While the information from EM-1/DASA 1200 is adequate for certain cases, it gives little guidance for target situations of current interest (see Section 1.5 for examples). Furthermore, there is no differentiation between dust generation and air temperature rise. Reference 3, Volume I includes a discussion of a consistent geophysical soil description useful for predicting soil blowoff response. Information in Table 4 is taken from that work.

An improved methodology begins with target selection and proceeds to geophysical description. A breakdown of key geophysical descriptors is given in Table 4. The last section of the table deals with upper horizon characteristics that dominate the type of thermal layer description found in EM-1/DASA 1200. However, it is important to consider other factors of general and subsurface nature for a complete description. Illustration of this point is given in reference to an abbreviated summary of the results of a series of solar furnace irradiation tests on bare soil samples of selected non-ideal surfaces, Table 5. Differentiation of the

Table 3. SUMMARY OF INFORMATION FOR DETERMINING SURFACE THERMAL RESPONSE BASED ON EM-1 AND DASA 1200

EM-1 CATEGORIES	EM-1 SUBCATEGORIES	MODIFYING COMMENTS FROM EM-1 AND DASA 1200	COMMENTS, THIS WORK
Thermally near ideal	Water*	Calm water only, rough water may be non-ideal	
(Precursor unlikely;	Ground covered by white smoke layer*	High albedo shields ground	
Listed in order of certainty)	Heat-reflecting concrete	Low thermal absorption	Explosive decomposition of bound water may occur at high fluxes
	Frozen tundra, ice packed soil	High heat capacity	
	Moist soil sparse vegetation**	As above	If soil excess moisture is driven out by thermal pulse, surface may become non-ideal
	Commercial and industrial areas	Density of buildings prevents continuous thermal layer development	
Thermally non-ideal	Desert sand*	"Popcorning" from NTS surface is used as evidence.	NTS surface is Alluvial Playa not desert sand**
(Precursor likely;	Coral*		
	Asphalt*	High heat absorption	
listed in order of certainty)	Surfaces with low, thick vegetation	Outgasing of vegetation can cause thermal layer. If vegetation is tall, surface is near ideal.	
	Surfaces covered with dark smoke layer*	High heat absorption	
	Dark colored rock	As above	
	Agricultural areas, residential areas		
	Dry soil, sparse vegetation**		

---

* Atmospheric nuclear test data support this conclusion.

** Surfaces of this type were studied in a program of solar furnace irradiation tests.

Table 4. SUMMARY OF GEOPHYSICAL SURFACE DESCRIPTION METHODOLOGY

MAIN CATEGORY	SUB-CATEGORY	EXAMPLES
General	Geography Terrain	Mid-latitude steppe, mountain
Subsurface Properties	Formation	Alluvial
	Chemical composition	Quartz
	Physical properties	Grain size, heat conductivity
Upper Horizon	Surface characteristics, geological	Playa, top soil
	Optical	Albedo in percent
	Moisture content	Value in percent
	Vegetation	Sparse, grass, trees
	Cover	Tundra, snow, ice
	Improvements	Roads, buildings

Table 5. SOLAR FURNACE IRRADIATION TEST RESULTS ON BARE SAMPLES OF NON-IDEAL SURFACES

DRY SURFACE	AIR HEATING*	DUST GENERATION*	MODIFICATIONS DUE TO MOISTURE
Alluvial Playa (including NTS)	High	Moderate	Role of moisture is complex, may increase or decrease dust generation depending on particular site
Clay soils	Moderate	Very intense	Small
Sandy soils	Small	Small	Major — depends on moisture to produce blowoff
Top soils Eastern U.S.	Moderate	Small	Moderate
Top soils Northwestern U.S.	High	Small	Moderate
"Ideal Surface"	Low	Low	None

* For quantification of these values see Table 2, Volume I Reference 3.

effects of air heating, dust generation, and moisture is included. Note the striking differences among the non-ideal surfaces studied and, in some cases, the site dependency observed for a given surface type. While the results illustrate an improvement over use of EM-1/DASA 1200 rules-of-thumb, a systematic method for identification of non-ideal effects (i.e., dust, thermal rise, etc.) is required. That method is the thermal layer modeling that forms the bulk of this report.

1.4 NON-IDEAL BLAST WAVE BEHAVIOR

The subject of air blast and, in particular, non-ideal effects associated with thermal layer development are discussed in a number of references, including EM-1/DASA 1200. (See References 1 through 5 and references quoted therein). The salient points are outlined here to provide an overview, and the reader is referred to the original works for further information. Non-ideal air blast occurs over thermally non-ideal surfaces for a specific range of weapon yields, HOB's and ground ranges. The following bounding parameters cover the observed (at NTS) regions of non-ideal effects: yield, 1-60KT; HOB, 100 to 600 scaled feet; range, 150 to 1100 scaled feet (see Figure 6, Volume I, Reference 3). The properties of the non-ideal blast wave that are of interest are the reduced static pressure, the increased dynamic pressure, and the enhanced dust loading of the air behind the shock, when compared to an ideal wave. The purpose of a thermal layer model is to generate realistic initial conditions that allow calculation of non-ideal blast wave behavior of target structures. That the difference between ideal and non-ideal blast wave behavior is large can be appreciated by a comparison of major effects under the two conditions as was shown in Table 1. In summary, it apparent that large variations in weapons effects will occur depending on the surface nature. The desire to quantify the effects and reduce the overall uncertainties motivates the present work.

1.5 SYSTEMS INTERESTS IN NON-IDEAL SURFACES

To illustrate the important questions that remain in non-ideal surface specification and to provide focus for this work, we have surveyed a number of current systems needs for information. Table 6 relates these needs to our present knowledge, and illustrates important areas as when data are inadequate. To summarize, one needs a better method of judging non-ideal surface conditions for a wider geophysical surface set than previously encountered, for weapon yields both below and above those encountered in the data. Cover and moisture, both vegetation and precipitation, need to be explored. Other surface materials, such as concrete, asphalt, roofing material, and the like need to be studied. Thermal layer development and blast wave propagation in and among foilage, trees and buildings should be quantified.

1.6 TECHNICAL APPROACH

The plan to meet the goals outlined in the preceding sections involves three basic steps:

- Review and analyze existing data related to thermal layer development
- Develop a thermodynamic model based on observables
- "Cross check" the model, i.e., how well does the model based on soil blow-off data agree with NTS data.

As has been argued above, a first-principles thermo- and hydro-dynamic model of the thermal layer development is difficult due to the complexity and intractability of the problem. Thus the model development started from observables, and hence the first task is to refine these observables. Prior work had developed some thermal layer data from atmospheric test shots. Procedures developed during the first phases of this contract allowed a methodology to,be developed

Table 6. EXAMPLES OF PROGRAM-RELATED INTERESTS IN THERMAL LAYER DEVELOPMENT

PROGRAM	SYSTEM INTEREST	GEOPHYSICAL SOIL DESCRIPTION	SOIL CONDITIONS	KEY THERMAL LAYER PARAMETERS	COMMENTS
NTS VERIFICATION — IMPROVED KNOWLEDGE OF NON-IDEAL EFFECTS	• Interpolate precursor formation conditions • Experimental verification of overpressure and dynamic pressure waveform	• Alluvial fan or playa • Desert	• No vegetation • Usually very dry and dusty, but some shots after rain or floods	• Height and temperature in thermal layer for low yields • Dust in thermal layer leading to increased dynamic pressure	• Known to be a non-ideal surface • Tests reveal site differences in surface response, especially with regard to moisture.
MINUTEMAN	• Verification of structural hardness to non-ideal blast waves	• Mixed geological origins, mid-latitude steppe	• Vegetation is frequently present	• As above, but for large yields	• Little dust generation but strong air heating discovered in tests.
TRIDENT-POSEIDON	• Dust sweep up in stem leading to fratricide	• Mixed — geological origin mostly — humid planes, mid-latitude	• Very frequent snow cover. • Vegetation	• Dust loading of layer for TRIDENT HOB and yield	• Most likely near ideal surfaces, especially with respect to dust generation.
MX	• System hardness validation environment	• Alluvial fan or playa • Desert	• Probably no vegetation • Moisture and snow cover must be studied parametrically	• As above (NTS), but for threat range, yields and HOBs at or near hardness limit for ideal blast wave conditions	• Site-specific tests need to be made (see NTS).
ABM	• Radar return from sweep up dust	• As MINUTEMAN	• As MINUTEMAN	• Dust loading at threat HOB, yield	• Extrapolation to high yields needs to be done via model.
THEATER NUCLEAR WEAPONS	• HOB for max static and dynamic pressure; collateral damage tradeoff	• As MINUTEMAN	• As MINUTEMAN	• Soil conditions that cause precursor	• Surfaces are complex in terrain and improvements.

that evaluates thermal layer temperatures from all precursor developing airburst tests. Thus the first step consisted of extracting thermal layer temperatures from Nevada Test Site (NTS) atmospheric test shot data. The specific tasks performed were as follows:

1) Review previous data on cloud radial development.
2) Establish an empirical formulation for radial position as a function of time, the allowed free parameters being yield and HOB.
3) Differentiate this expression to obtain radial velocity and compare the "global" predictions versus specific shots, especially Priscilla.
4) Obtain equivalent layer temperatures from the shock velocity assuming the shock relationship and a constant γ (see page 2-3)
5) Compare these "backed out" temperatures with actual measured temperatures, and simulation results.

The goal of this task effort is the complete specification of the thermal layer temperature for NTS soils and over NTS yields. It will still be inadequate in the following respects:

- Extrapolation of yields greater than about 50KT
- Use on other soil surfaces.

To correct these inadequacies a modeling effort was undertaken. This effort has as its basis a large body of theoretical investigations on thermal layer behavior developed under other SAI contracts (References 1 and 2) as well as work by other groups (References 6 and 7). The previous work had modeled thermal layer formation over dry, dusty soils, but due to the parametric nature of the assumptions, virtually any desired layer temperature could be calculated given the proper set of starting assumptions in key variables. In addition, significant new data were available from a 2-year series of solar furnace irradiation tests. These data allowed for the first time a close examination of thermal layer development, particularly from high-speed photographic films made of the tests. With this information, a theoretical model that avoided some of the pitfalls encountered earlier was built which predicts the most important parts of the layer development. In particular, these new efforts were designed to:

- Include the new experimental data on soil blowoff where a direct calculation of the particular feature was not feasible.
- Include in the model the physical processes observed to take place in the tests.
- Adapt the calculation to take account of the "feedback" in the process, whereby each step is modified by the prior time history.
- Avoid unnecessary dependency on arbitrary parameters either physical or calculational.

A simplified flow chart of the generic method is shown in Figure 2. Note that calculation is of an unstable, transient phenomenon, and the method includes the feedback of information to properly control the process. The model is expected to compute air heating and thus air temperature (using the air equation of state), particle dust loading, and heat lost to subsurface conduction and to heat reflection. This simplified diagram only touches on the main points and ignores others completely (i.e., the role of water in the soil). These points will be treated later as warranted.

In conclusion, a methodology was set up using the best of the theoretical and experimental information available, to calculate thermal layer development (i.e., both temperature and dust loading) for a wide range of yields and soil types. A summary view of the overall program methodology is provided in Figure 3.

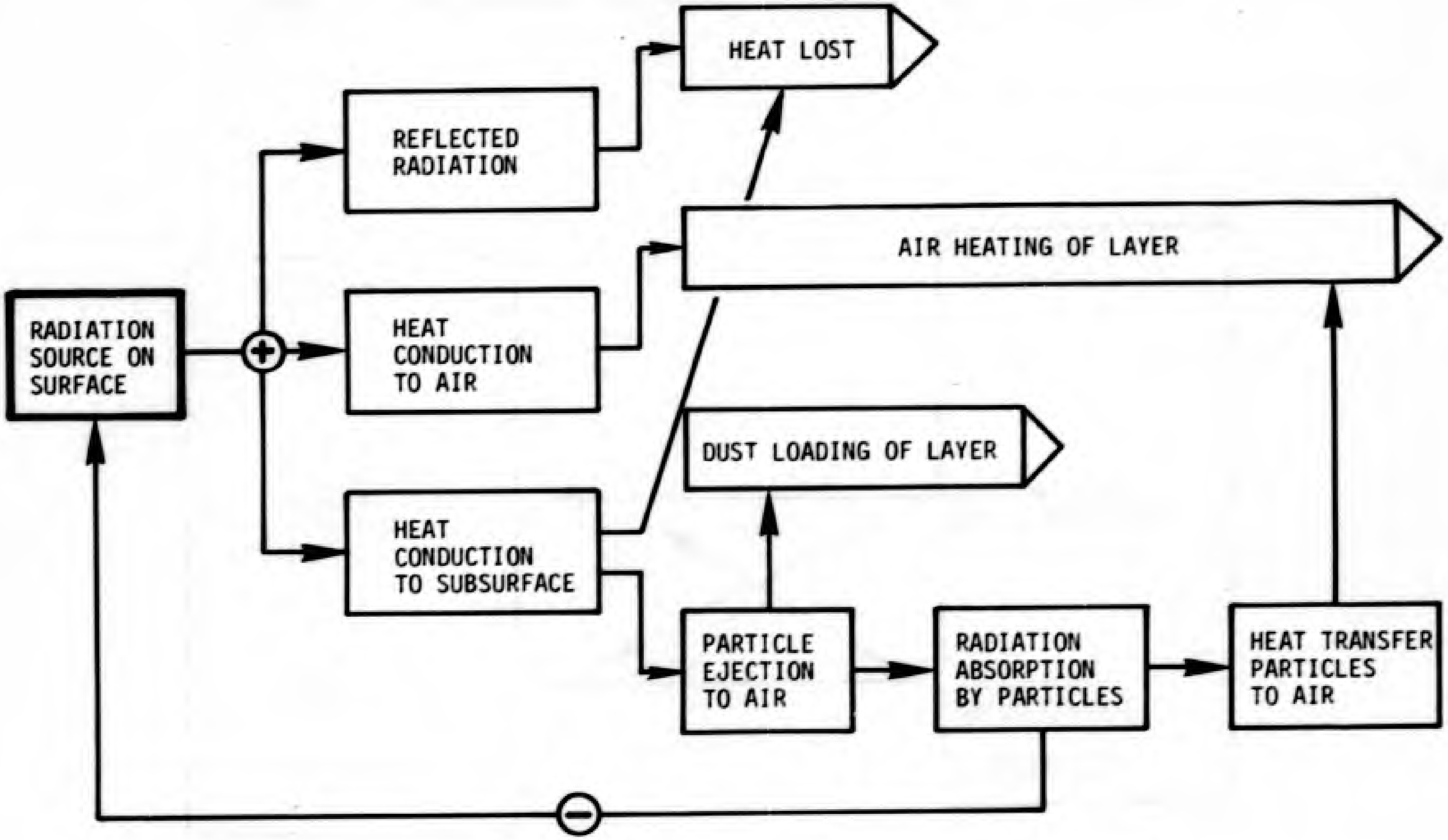

Figure 2. Simplified Schematic Diagram of Calculational Procedure — Soil Blowoff Analysis

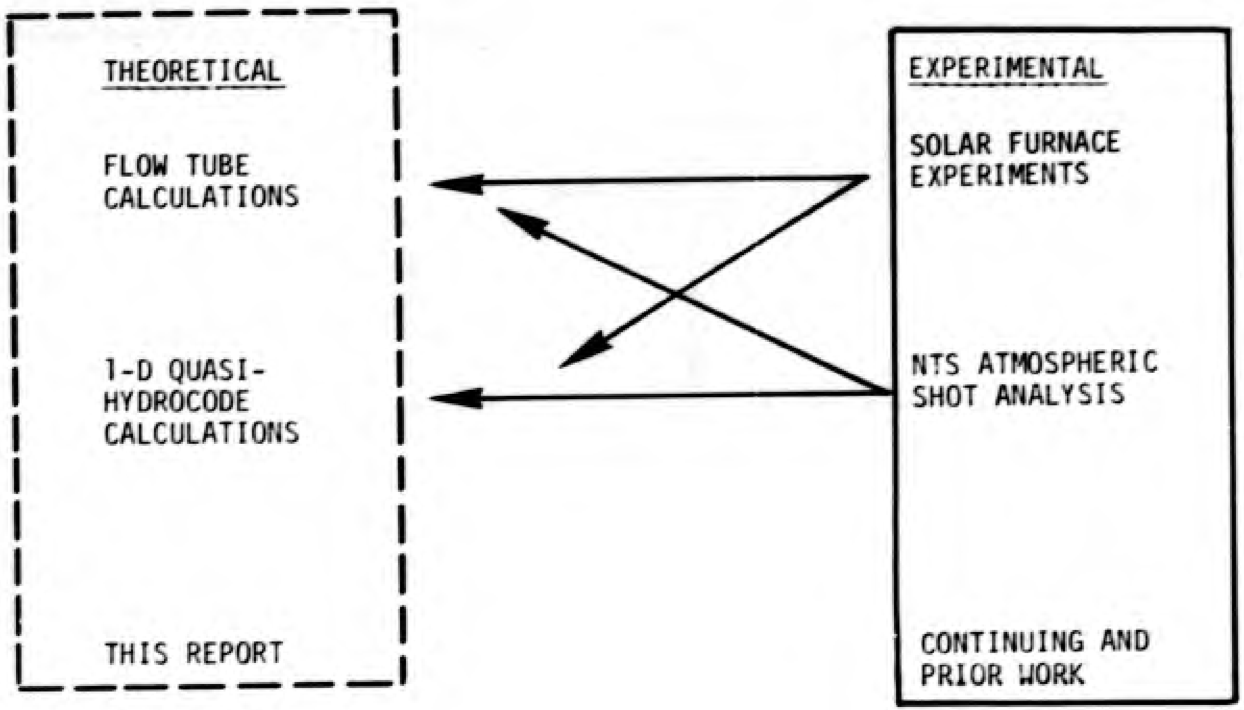

Figure 3. Interrelation of Programs in Thermal Layer Investigation

Section 2

THERMAL LAYER TEMPERATURES FROM NTS TESTS

2.1 METHOD

The extraction of preshock thermal layer temperatures from NTS test data requires knowledge of the shock equations. In this section we briefly review the fundamentals of the shock equations, and show how the relevant data were obtained from NTS data.

The derivation of the necessary equations of shock behavior begins with the assumption of isentropic flow of a perfect gas. We shall sketch here the essential steps and assumptions. Several excellent references texts are available for further details (References 8 and 9). The following laws can be stated at the outset (see Table 7 for symbol definitions).

First Law of Thermodynamics	$h_o = h + \frac{v^2}{2}$
Equation of Continuity	$\frac{\omega}{A} = \rho v$
Definition of Mach Number	$M \equiv v/c$
Conservation of Linear Momentum	$p_o + \frac{\omega}{A} v_o = p + \frac{\omega}{A} v$
Equation of State of a Perfect Gas	$pV = RT \quad p = \rho RT$
Equation for a Perfect Gas undergoing Reversible Adiabatic (isentropic) Processes	$pV^{\gamma} = \text{constant}$
Enthalpy Change in a Perfect Gas	$\Delta h = C_p \Delta T$

Table 7. SYMBOLS USED IN SHOCK EQUATIONS

SYMBOL	
h	enthalpy per unit mass
v	net velocity
ω	mass flow rate
A	area
p	pressure
T	temperature
V	volume
ρ	density
C_p, C_v	specific heats at constant pressure, volume
R	gas constant
M	particle velocity
W	shock velocity
C	sonic velocity

Also for a Perfect Gas

$$C_p - C_v = R$$

$$C_p/C_v \equiv \gamma$$

$$C_p = (\gamma/\gamma-1)R$$

Sonic Velocity

$$c = \sqrt{\gamma RT} = \sqrt{\gamma/pv}$$

In addition, we must define the coordinate frame for the shock, which is a one-dimensional system under the present approximations. Figure 4 defines the system. Compressible gas in region two, flowing with particle velocity u_2 toward the right, creates a discontinuity at the boundary of region 1. The discontinuity, a shock, moves with relative velocity with respect to region 1.

Under the assumptions of isentropic flow we may calculate, for a reference system of no net velocity (stagnation frame denoted by subscript o) relative to any frame of net velocity v:

$$h_o = h + \frac{v^2}{2}$$

$$v = \sqrt{2(h_o-h)} = \sqrt{2\ C_p(T_o-T)} = \sqrt{2\gamma R(T_o-T)/(\gamma-1)}$$

This can be rewritten as

$$\frac{T_o}{T} = 1 + \frac{v^2}{2C_pT} = 1 + \frac{\gamma-1}{2}\left(\frac{v}{c}\right)^2 = 1 + \frac{\gamma-1}{2}M^2$$

when T is the temperature of the system of net velocity v and T_o is the temperature in the stagnation frame. In other words, T_o is the total temperature, or the temperature a probe would measure if the flow were brought to rest in the probe's reference frame. The net velocity v is the fluid particle velocity in the absence of shocks, and is given by the formula for the respective frames as shown in Figure 4 when shocks are present.

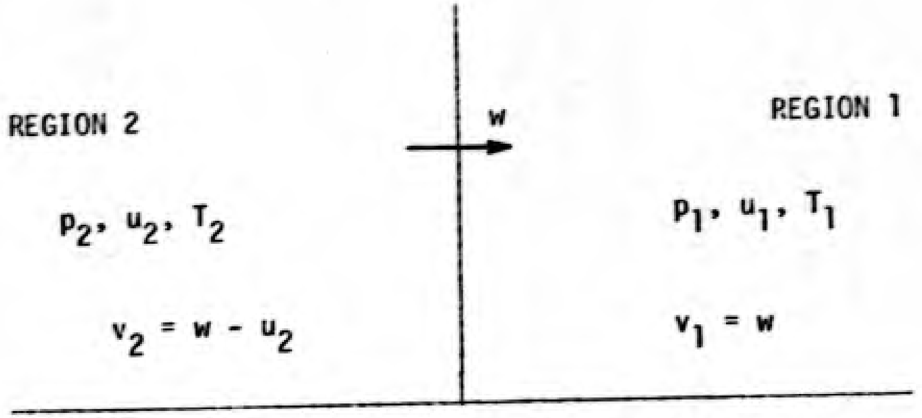

v = net velocity in steady flow frame, i.e., shock is stationary

Figure 4. Coordinate System Definition for a Right-Moving Shock

If we add the assumption of the equation of state of a perfect gas to the requirement of isentropic flow, we can arrive at pressure and density relationships for the stagnation state. Writing $pV = RT$ (perfect gas) and

$$pV^{\gamma} = \text{constant (isentropic perfect gas)}$$

using $\rho = 1/V$ we obtain

$$p \doteq \rho^{\gamma}$$

$$\frac{p}{p_o} = \left(\frac{\rho}{\rho_o}\right)^{\gamma} = \left(\frac{RT_o p}{RT p_o}\right)^{\gamma}$$

$$\frac{p}{p_o} = \left(\frac{T_o}{T}\right)^{\gamma/\gamma-1}$$

$$\frac{T_o}{T} = \left(\frac{p}{p_o}\right)^{\gamma-1/\gamma}$$

Now returning to the relationship between stagnation temperature ratio and net velocity, we have

$$\frac{T_o}{T} = 1 + \frac{\gamma-1}{2} M^2$$

$$\frac{p_o}{p} = \left\{1 + \frac{\gamma-1}{2} M^2\right\}^{\gamma/\gamma-1}$$

$$\frac{\rho_o}{\rho_o} = \left\{1 + \frac{\gamma-1}{2} M^2\right\}^{1/\gamma-1}$$

for isentropic flow of a perfect gas.

Now let us consider the presence of a shock wave (refer to Figure 4). Under the assumption of isentropic conditions at the shock front, we have from the first law of thermodynamics:

$$2\,C_pT_1 + v_1^2 = 2\,C_pT_2 + v_2^2 = 2\,C_pT_o.$$

Thus the stagnation temperature in region 1 and 2 is identical under these assumptions.

Because of this fact we may write immediately

$$\frac{T_2}{T_1} = \left[\frac{1 + \frac{\gamma-1}{2}M_1^2}{1 + \frac{\gamma-1}{2}M_2^2}\right]$$

but $$\frac{T_2}{T_1} = \frac{p_2\rho_1}{p_1\rho_2}\,.$$ for perfect gases

and $$\frac{T_2}{T_1} = \frac{p_2v_2}{p_1v_1}$$ by the equation of continuity

thus $$\frac{T_2}{T_1} = \frac{p_2M_2C_2}{p_1M_1C_1}$$ or

$$\frac{T_2}{T_1} = \left(\frac{p_2M_2}{p_1M_1}\right)^2$$

since $M = v/c$, and $C^2 \doteq T$.

We therefore can write

$$\frac{p_2}{p_1} = \frac{M_1}{M_2}\,\frac{\left(1 + \frac{\gamma-1}{2}M_1^2\right)^{1/2}}{\left(1 + \frac{\gamma-1}{2}M_2^2\right)^{1/2}}\,.$$

Let us now consider the conservation of linear momentum at the shock interface

$$p_1 + \frac{\omega}{A} v_1 = p_2 + \frac{\omega}{A} v_2$$

which becomes

$$p_1 + \rho_1 v_1^2 = p_2 + \rho_2 v_2^2$$

after using the continuity equation. Now for a perfect gas

$$p = \frac{\rho RT}{\gamma} = \frac{\rho C^2}{\gamma} = \frac{\rho v^2}{\gamma} M^2$$

Substituting in the equation for momentum conservation we have

$$p_1 \left(1 + \gamma M_1^2\right) = p_2 \left(1 + \gamma M_2^2\right)$$

$$\frac{p_2}{p_1} = \frac{\left(1 + \gamma M_1^2\right)}{\left(1 + \gamma M_2^2\right)} .$$

Previously, we showed that, based on the first law of thermodynamics, an alternative relation for the pressure ratio held. Equating the result of the conservation of linear momentum to that of the first law of thermodynamics gives

$$\frac{M_1 \left(1 + \frac{\gamma-1}{2} M_1^2\right)^{1/2}}{\left(1 + \gamma M_1^2\right)} = \frac{M_2 \left(1 + \frac{\gamma-1}{2} M_2^2\right)^{1/2}}{\left(1 + \gamma M_2^2\right)}$$

the solution of which yields:

$$M_2^2 = \left(\frac{M_1^2 + \frac{2}{\gamma-1}}{\frac{2\gamma}{\gamma-1} M_1^2 - 1}\right) .$$

Substitution in the above expression gives:

$$\frac{p_2}{p_1} = \frac{\left(1 + \gamma M_1^2\right)}{1 + \gamma \left(\frac{M_1^2 + \frac{2}{\gamma-1}}{\frac{2\gamma}{\gamma-1} M_1^2 - 1}\right)}$$

$$= \frac{2\gamma}{\gamma+1} M_1^2 - \frac{\gamma-1}{\gamma+1} .$$

Defining $p_2 = p_1 + \Delta_p$, we obtain

$$\frac{\Delta p}{p_1} = \frac{2\gamma}{\gamma+1} \left(M_1^2 - 1\right) .$$

The above equation applies to the conditions of shock propagation in a perfect gas, under the assumption of the first law of thermodynamics, the conservation of linear momentum, and isentropic flow at the shock interface.

If p_1, Δ_p, γ are known,

$$M_1^2 = \left(\frac{\gamma+1}{2\gamma} \frac{\Delta p}{p_1} + 1\right) \text{ and } T_1 = \left(\frac{v_1^2}{\gamma R M_1^2}\right) .$$

Thus knowledge of v_1, the propagation velocity of the shock in region 1, in addition to the knowledge of the variables stated above, yields T_1, the temperature of region 1 into which the shock is propagating, when the stated conditions and assumptions are valid. This method of temperature determination is called the overpressure method.

Since we know these equations must hold, for each instant of time the above equation ought to give valid temperatures. Unfortunately, the body of knowledge from a series of WT reports on the various NTS shots indicated that the use of the overpressure method was invalid for extracting temperature data. We shall later present data to dispute this contention, however. The reason that the overpressure method failed to give realistic temperatures when used by the authors of the various WT reports written to summarize the NTS data is a misapplication of a shock angle correction. Photographic data often allowed viewing of the angle of the shock wave with respect to the ground surface <u>above the thermal layer</u>. However, the overpressure method relates to the fact the shock is normal exactly at the surface inside the layer — a region not seen photographically. Two other methods were attempted in the WT report series. One assumes sonic wave propagation in the thermal layer and would demand $\Delta p \rightarrow 0$. This is manifestly untrue, and would yield very high temperatures if applied. The various WT reports generally agree on this point. A third method, also involving the angle of the shock fronts, is used in most work in the NTS series to extract temperatures. This method necessitates viewing the shock, a tricky experimental circumstance, but requires the shock angle above the layer in contrast to the first method. However, several shots are documented where these data were available and reasonable values of temperatures recorded.

Information on v_1 from a wide variety of NTS shots is not available, particularly for the small increments of time and space needed to obtain the temperature. The instantaneous radial extent of the dust cloud was available because of the efforts on previous contract work (References 1 and 2). The differentiation of the expression for the radial position, with respect to time, yields the instantaneous velocity of the leading edge of the dust cloud along the ground surface. The final assumption necessary to complete the problem is that the instantaneous velocity of the leading edge of the dust cloud is identical to that of the leading edge of the shock. This is a reasonable assumption but cannot be proved independently from first principles. To test the value of the equations, assumptions, and methods described here, we have made a calculation for a specific NTS shot: Plumbob-6, Priscilla, 36.6KT at 700 feet. Table 8 illustrates the results of application of utilization of the results of the theoretical analysis. Specifically, for a $\gamma = 1.4$, air at STP, we obtain

$$M_p = \left(\frac{0.857\ \Delta p_p}{p_o} + 1\right)^{1/2}, \quad T_p = \frac{v_p^{\ 2}}{4324\ M_p^{\ 2}} \qquad \text{(A)}$$

Where M_p is the Mach number of the shock entering the thermal layer, p_o is the ambient atmospheric pressure in the layer, Δp_p is the maximum rise of overpressure in the precursor pulse (i.e., before main shock front arrival), v_p is the velocity of the precursor wave entering the thermal layer. Referring to the table and graph of temperatures versus ground range, Figure 5, we can now demonstrate the validity of the assumptions used previously:

A) Comparison of shock and dust cloud times of arrivals and velocities shows that although the dust cloud lags the shock as anticipated, the dust cloud frontal velocity is approximately equal to that of the shock. Thus, the use of dust velocity as a measure of shock velocity is a justified procedure.*

---

* Refer to page 28, Reference 1, for more detailed discussion of dust shock lags.

Table 8. AN EXAMPLE CALCULATION FOR SHOT PRISCILLA (PLUMBOB-6)

T_o = 290.7°K, P_o = 13.2 psi

GROUND RANGE* (ft)	PRECURSOR ARRIVAL TIME* (sec)	PRECURSOR VELOCITY* (ft/sec)	DUST ARRIVAL TIME** (sec)	DUST VELOCITY (ft/sec)	Δp IN PRECURSOR* (psi)	T CALCULATED* (°K)$^+$	Mp CALCULATED	T LAYER CALCULATED (°K)
550	0.116	7600			39.2	3000		3767
650	0.131	6600			31.4	N/A	1.74	3315
750	0.146	6300			26.0	3800	1.64	3414
850	0.163	5700	0.172		25.6	2850	1.63	2822
1050	0.201	4700	0.213	4878	20.6	N/A	1.53	2185
1350	0.268	4150	0.274	5000	12.1	1960	1.34	2230
1650	0.350	3200	0.362	3409	15.7	N/A	1.42	1172
2000	0.475	2300			14.2	1050	1.39	636

---

*Source: WT 1403

**Source: References 1 and 2

$^+$Angle of fronts method used

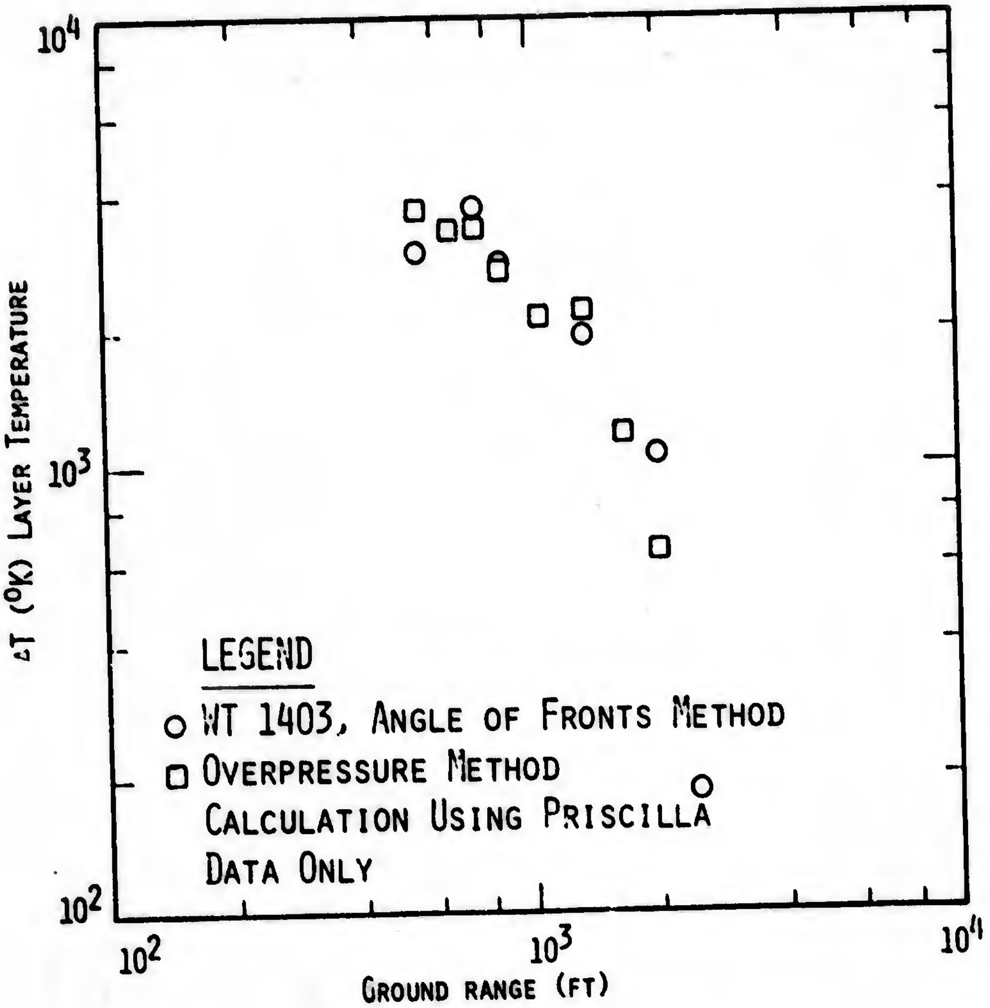

Figure 5. Comparison of Thermal Layer Temperatures for Shot Priscilla Overpressure Method versus Angle of Fronts Method

B) Use of Equation A to derive thermal layer temperatures gives excellent agreement with temperatures extracted from NTS data as presented in the appropriate WT reports. In particular, we show that use of the formula for a shock normal to the ground surface at the bottom of the thermal layer is well justified. Use of the shock angle as viewed above the thermal layer as was used in the WT reports is incorrect on the basis both of physics,* and on agreement with the data. Thus the shock equations and numerical evaluations are valid.

C) The sensitivity of Equation A to values of v and Δp is not severe — we find

$$\frac{\Delta v}{v} = 2\frac{\Delta T}{T} \quad \text{and} \quad \frac{\Delta(\Delta p)}{(\Delta p)} = 0.6\frac{\Delta T}{T} .$$

Furthermore, inspection of the overpressure records for these ground ranges shows no particular problem existed in identifying Δp, the peak precursor pressure. The "noise" in the precursor region appears small in all records for these ground ranges.

In conclusion, we have developed and demonstrated a method that will allow determination of the average thermal layer temperature as a function of ground range for NTS test shot Priscilla.

2.2 RADIAL SHOCK VELOCITY FITS

The method described in Section 2.1 requires radial shock velocity predictions for arbitrary HOB and yields. In order to extract this from NTS atmospheric shot data, fits to the extent of the dust cloud as a function of time are required. At the beginning of the present effort, prior work was reviewed for applicability. In

---

* That the shock must be normal to the ground at the ground-air interface is required by the subsequent propagation path-radial, and is further required for the "clean up" process to occur.

Reference 1 an expression for the radial dimension R of the precursor dust cloud was given which has a very good fit to 29 NTS precursor shots in terms of HOB and yield. Fit errors were well under 10 percent. Pages 68 and 69 of Reference 1 display this formula. Unfortunately, this expression is complicated and has several points of inflection between regions of validity in t, and HOB. Despite the difficulty of handling this expression, it was differentiated and used to calculate preshock thermal layer temperatures in Reference 2. Such temperatures were used to successfully compute post-shock air densities and precursor pressures. No conclusive evidence for the physical mechanism responsible for the temperature was apparent, however.

As part of the present work the radial extent of the dust layer was reinvestigated, and an expression was developed parameterizing the dust location on the ground in terms of slant range S. It was found that

$$S = S_p \tanh \left[({}^{t}/t_p)^{\beta}/\alpha \right]$$

with S_p = slant range at precursor formation

t_p = time of precursor formation

t_s = time of precursor separation

$\alpha = 1/\tanh^{-1} (S_p/S_s)$

β = fitting constant

S_s = slant range at precursor separation

gave acceptable fits over the entire range t_p to t_s rather than requiring different formulae for two regions within this range as had been the case previously.

Differentiation of the expression for S with respect to time, and projection onto the ground surface (ground range = χ) yields

$$v_p = \frac{S S_s \beta}{\chi t_p \alpha^{1/\beta}} \frac{\left|1 - (S/S_s)^2\right|}{\left|\mathrm{Tanh}^{-1}(S/S_s)\right|^{1-\beta/\beta}}$$

with $S = (\chi^2 + HOB^2)^{1/2}$

and $\beta = 0.650 \left(\frac{\chi_p}{150\ \omega^{1/3}}\right)^{0.7131}$.

Also, we find that $\frac{S_s}{S_p} = 1 + 5 \left(1 - \frac{HOB}{670\ \omega^{1/3}}\right)$

for Yucca Flats, and

$$\frac{S_s}{S_p} = 1 + 5 \left(1 - \frac{HOB}{615\ \omega^{1/3}}\right)$$

for Frenchman Flats. The fits of S_s/S_p and β to HOB and yield were accomplished by a least-squares minimization technique. As a demonstration of the fit, and illustrative of the improvement realized, refer to Figure 6, where the precursor shock horizontal velocity versus ground range is plotted from test report data, from our previous fits, and from the current work. A considerable improvement is evident. Note also the measured dust velocity matches fairly well; an 0.96 correction appears to improve the situation.

Thus we have developed a functional form of the shock velocity in terms of HOB and yield. This formulation, when used in conjunction with the method developed in Section 2.1, allows the temperature of the thermal layer as a function of ground range, HOB, and yield to be determined.

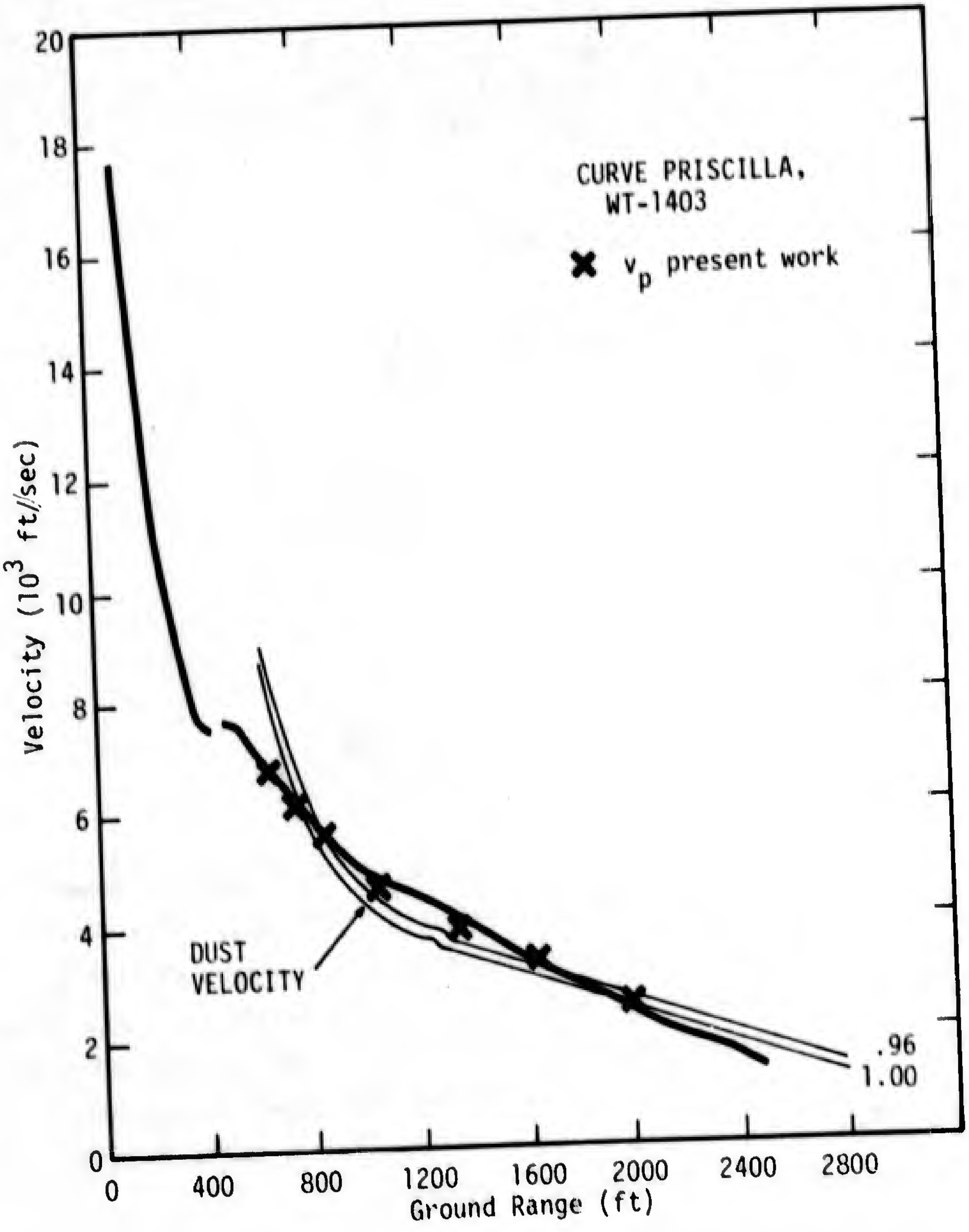

Figure 6. Horizontal Shock Velocity Versus Ground Range

2.3 TEMPERATURE OF THE THERMAL LAYER — NTS SHOTS

Following the development of the two preceding sections, we have calculated the thermal layer temperature rise $(T - T_0)$ as a function of ground range for 12 NTS atmospheric shots for which precursor overpressure records were adequate. In Table 9 we present these data along with certain other parameters such as calculated shock Mach number and predicted velocity of precursor. At this point, we have the tools to extend this analysis to investigate the rise in average layer temperature correlated with peak flux and fluence to shock arrival. It is in the analysis of these factors that trends may be observed that allow generalization of the temperature result. These will be described in the next section.

In summary, we have shown the average layer temperature calculated from a fit to precursor velocity as a function of HOB and yield. These temperatures agree well with temperatures measured during the tests, or inferred from the shock relations for that particular shot. These temperature values cover a wide range of HOB, yield, and thermal radiation parameters.

2.4 PARAMETERIZATION OF LAYER TEMPERATURE

The driving force behind the formation of the pre-shock layer is the thermal radiation. Calculation of peak flux and fluence to shock arrival for each station for the 12 prime NTS shots was made by the SAI code PREDUM (References 1 and 2). This is listed along with layer temperature for the 12 prime NTS shots of Table 9. We also calculate Q' the fluence above threshold

$$Q' = Q - Qth$$

Table 9. SUMMARY DATA ON NTS SHOT THERMAL LAYER TEMPERATURES AND RADIANT HEATING VALUES

SHOT, AREA AND CONDITIONS	GROUND RANGE (ft)	Q, FLUENCE TO SHOCK ARRIVAL (cal/cm²)	Q THRESHOLD (cal/cm²)	Q' = Q - Qth (cal/cm²)	φp, PEAK FLUX (cal/cm² sec)	$T - T_0$ LAYER TEMPERATURE RISE (°K)	$T - T_0/Q'$
ANNIE YUCCA FLATS	700	16.3	5	11.3	550	870.9	77.1
	900	25.0		20.0	478	905.1	45.3
	1050	28.4		23.4	344	644.3	28.4
	1150	28.7		23.7	266	577.9	24.4
TURK	1770	39.3	5	34.3	194	463.8	13.5
HORNET	630	38.6	15	23.6	492	629.5	26.7
	710	32.4		19.4	365	397.9	20.5
	840	24.2		9.2	236	199.8	21.7
	940	19.6		4.6	174	154.4	33.6
APPLE 1	1030	53.8	5	48.8	400	386.1	7.9
MOTH	670	29.1	17	12.1	337	332.6	27.5
	795	21.1		14.1	217	174.7	42.6
BEE	1060	39.1	5	34.1	258	334.4	9.8
CLIMAX	1552	128.7	32	96.7	419	843.6	8.7
	2011	91.0		59.0	256	401.0	6.8
DOG	608	151.7	20	121.7	829	1652.6	13.6
	974	105.8		85.8	501	1020.9	11.9
	1345	70.3		50.3	295	430.3	8.6
WASP PRIME	389	77.0	5	72.0	662	2538.8	35.3
	780	39.8		34.8	311	692.6	19.9
MET, FRENCHMAN FLATS (desert line)	750	25.4	5	20.4	686	839.6	41.2
	1000	36.9		31.9	525	972.5	30.5
	1500	32.3		27.3	176	550.0	20.2
PRISCILLA	650	73.3	15	58.3	1320	3234.8	55.5
	750	73.0		58.0	1156	2903.9	50.1
	850	74.0		59.0	1002	2380.3	39.1
	1050	76.4		61.4	712	1926.2	31.4
	1350	71.1		56.1	407	1664.7	29.7
	1650	56.9		41.9	249	912.6	21.8
	2000	41.4		26.4	150.5	530.0	20.1
GRABLE	675	69.7	5	64.7	1039	2238.2	34.6
	765	69.2		64.2	814	1827.1	28.5
	865	66.8		61.8	628	2308.8	37.4
	893	65.7		60.7	585	2102.2	34.6
	921	64.4		59.4	546	1771.6	29.8
	1170	49.2		44.2	308	934.7	21.1
	1419	35.6		30.6	188	768.6	25.1

and the normalized layer temperature

$$(T - T_0)/Q' = \Delta T/\Delta Q.$$

Note that $\Delta Q/\Delta T$ has the dimensions of entropy. We will discuss this interpretation later.

The values of Qth, the threshold fluence, were determined in the following way. If sufficient data for an individual shot were available, $T - T_0$ versus Q was plotted and the intercept $Q\ [(T - T_0) = 0]$ = Qth by definition. If insufficient data existed, the value of Qth taken from the solar furnace test data was used (Reference 3). The graphical method was used in Reference 2 with a set of temperature data that represented fits to the previously obtained precursor velocity formulation. In the present work we have improved considerably the velocity fits as was explained above, and recalculated Qth. It is interesting to note that major changes in Qth occurred for shots Hornet and Moth. Shot Hornet's value of Qth had been anomalously low in Reference 2 (see graph on page 72 for example). The present value is considered more consistent with the general trend of that graph, especially when shot Priscilla is added. We have summarized these data in Table 10, where we have also added a prediction of surface soil moisture content as developed from the methodology developed in the SAI analysis of solar furnace test data, Reference 3. The expectation is that for the nighttime desert conditions considerable condensed water or frost may be present, while during the daytime the ground should have relatively low surface moisture content (about 2 to 6 percent) unless local weather conditions dictate otherwise. Reference to Table 10 shows good correlation of expected and inferred surface moisture values. Figure 7 shows the values of thermal layer temperatures obtained by three methods: shock angle relationship as reported in WT 1403 Reference 9, our normal shock methodology but calculated for the radial velocity values of

Table 10. SHOT THRESHOLD FLUENCE AND SOIL MOISTURE CONTENT

SHOT	AREA*	Q THRESHOLD (cal/cm^2)	SHOT INITIAL CONDITIONS TIME (PST)	T_o (°C)	WEATHER CONDITIONS	SURFACE SOIL MOISTURE CONTENT (% BY WEIGHT) PREDICTED FROM SOLAR FURNACE DATA
CLIMAX	YF	32	0315	13.3		16
DOG	YF	20	0830	17.0	Heavy rain preceded shot	10
MOTH	YF	17		- 7.8		8
HORNET	YF	15	0515	- 1.0		7
PRISCILLA	FF	15	0630	17.5		7
REMAINING SHOTS	—	5	—	—		4

---

* YF = Yucca Flats, FF = Frenchman Flats

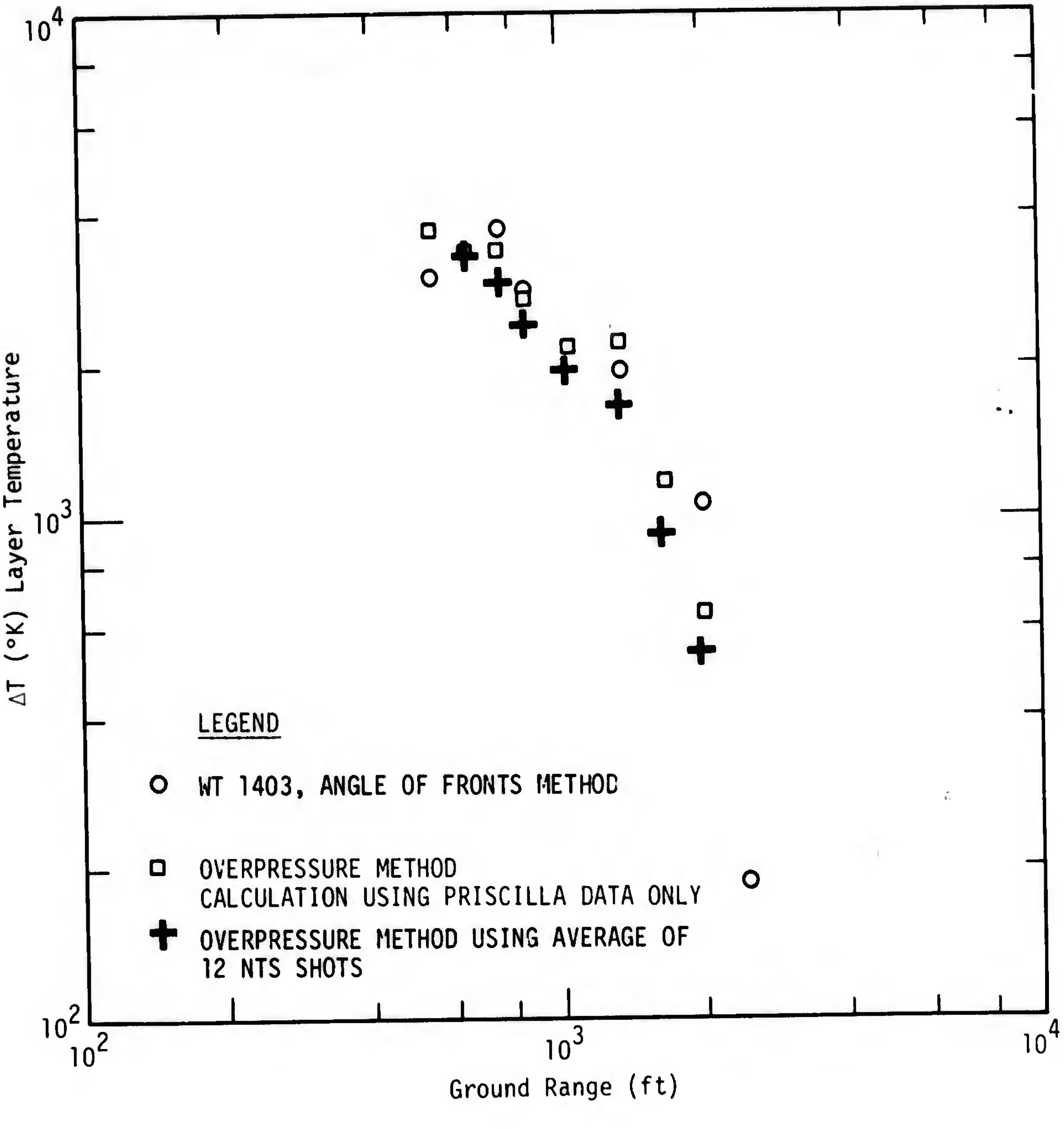

Figure 7. Layer Temperature as a Function of Ground Range for NTS Shot Priscilla

shot Priscilla as given in WT 1403, and our fitted estimates of temperatures based on 12 NTS shots using HOB and yield as free parameters.

In Figures 8, 9, and 10, we show $(T - T_0)/Q'$ versus Q', $\dot{Q}$ and $(T - T_0)$. Analysis of these graphs for trends has resulted in the following conclusions.

Concerning all three figures:

1) Yucca Flats data have considerable spread on a shot-by-shot analysis, but considerable uniformity among data for the same shot.

2) There is very little spread in Frenchman Flats data, however the HOB of the shots are similar.

3) Solar furnace test data show strong moisture-dependent blowoff effects for Yucca, and little or none for Frenchman. One may conclude the spread at Yucca was due to varying soil moisture conditions at shot time.

4) The moisture content of soils required to match the observed Q thresholds for the NTS shots is consistent and reasonable considering the corroborative data (see Table 10).

5) Values of 50°K/(cal/cm^{2}) for initial temperature rise of heated air for both Yucca and Frenchman soils were observed from the solar furnace tests. This value agrees well with the NTS data for the developed layer. This indicates that the subsequent volumetric heating closely matches the initial (partly conductive and partly volumetric) heating rates.

Concerning Figure 8:

6) The observation that fluence is a good scaling variable for thermal layer data is corroborated in NTS shot data. This scaling had been seen previously in the solar furnace test analysis; however, the present work allows a more general statement to be made due to the larger range of flux, temperature, and time development of the layer.

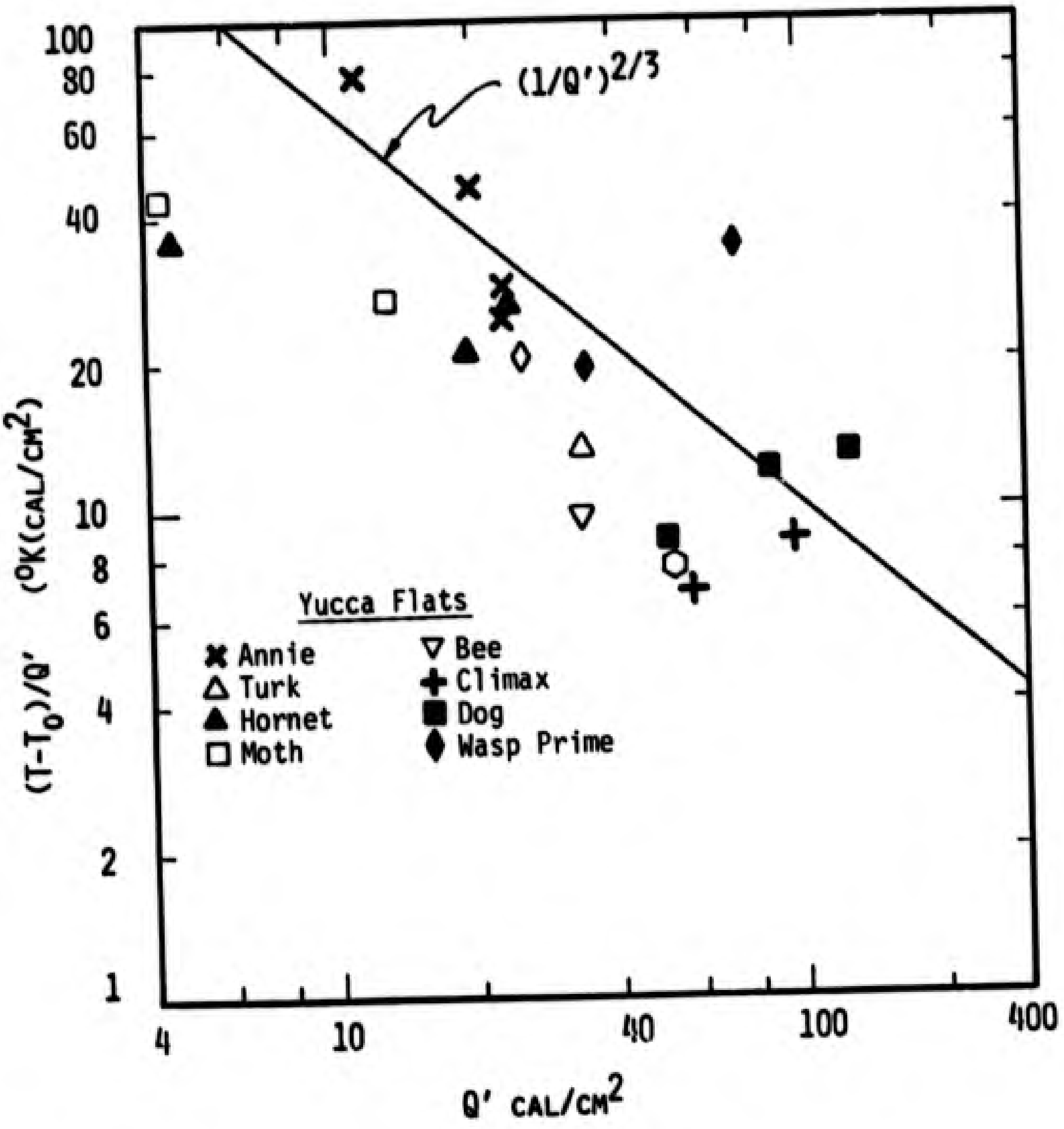

Figure 8a. A Normalized Layer Temperature Rise Versus Peak Fluence (Yucca Flats Data)

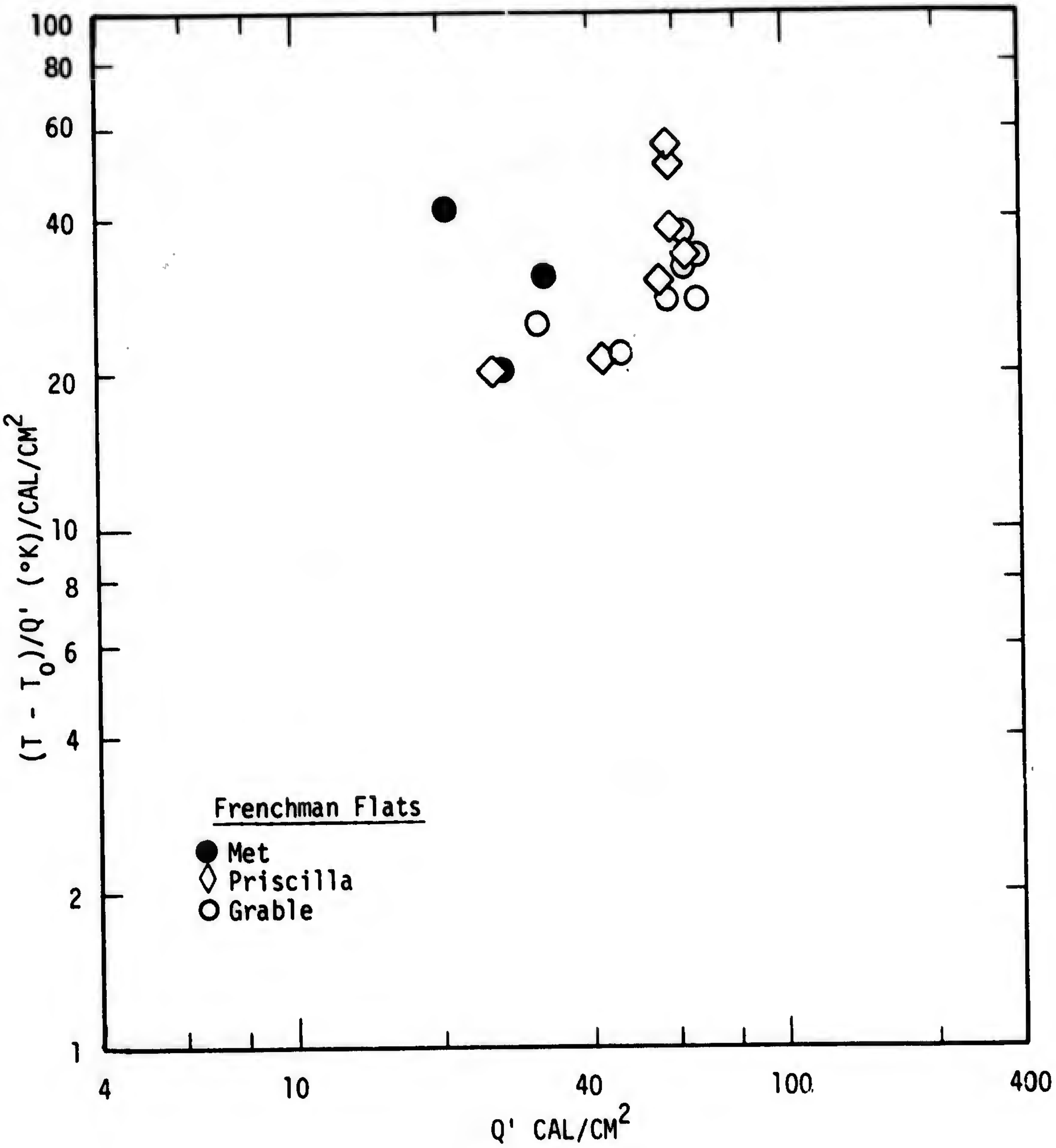

Figure 8b. A Normalized Layer Temperature Rise Versus Peak Fluence (Frenchman's Flats Data)

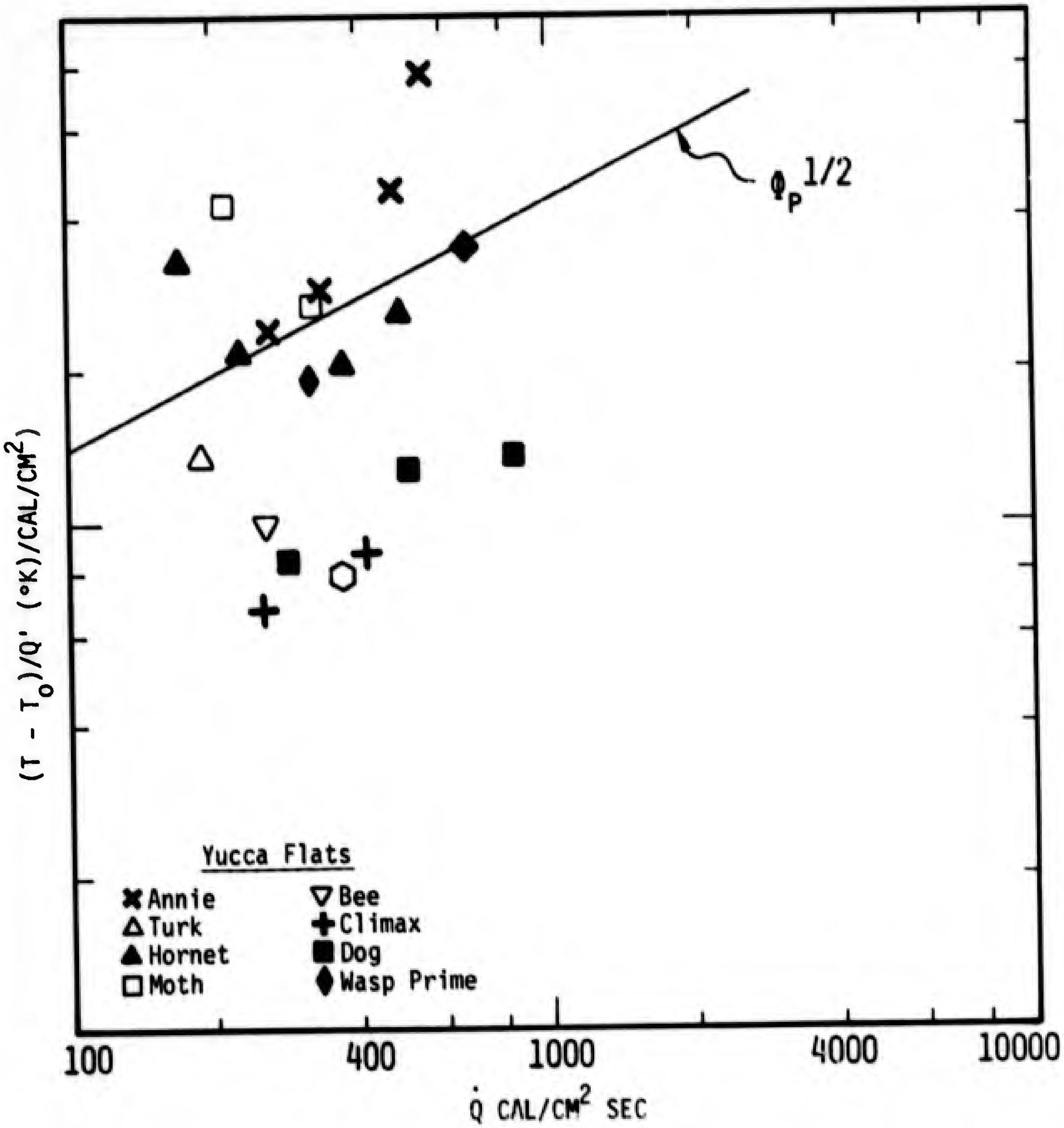

Figure 9a. Normalized Layer Temperature Rise Versus Peak Flux (Yucca Flats Data)

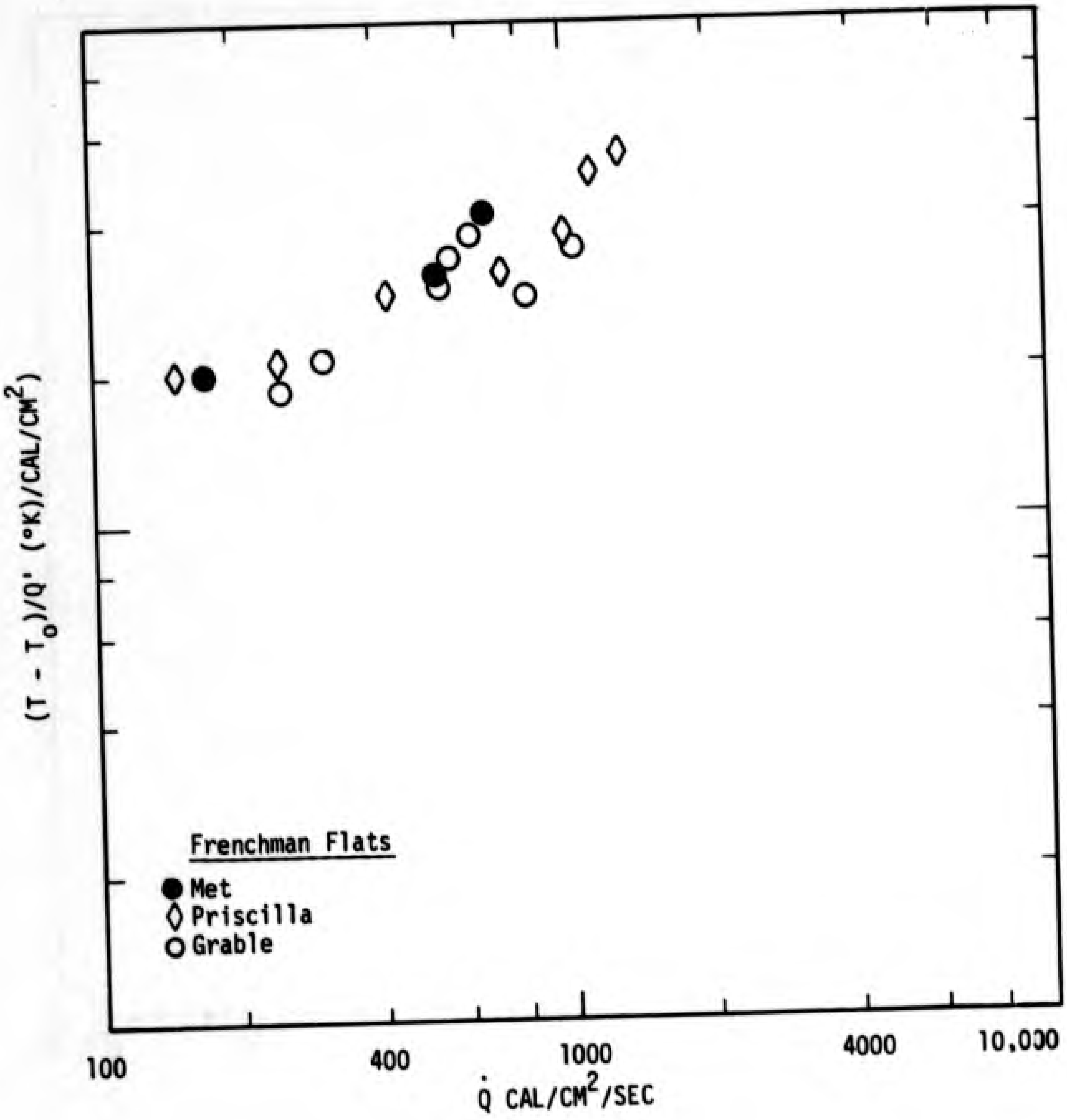

Figure 9b. Normalized Layer Temperature Rise Versus Peak Flux (Frenchman's Flats Data)

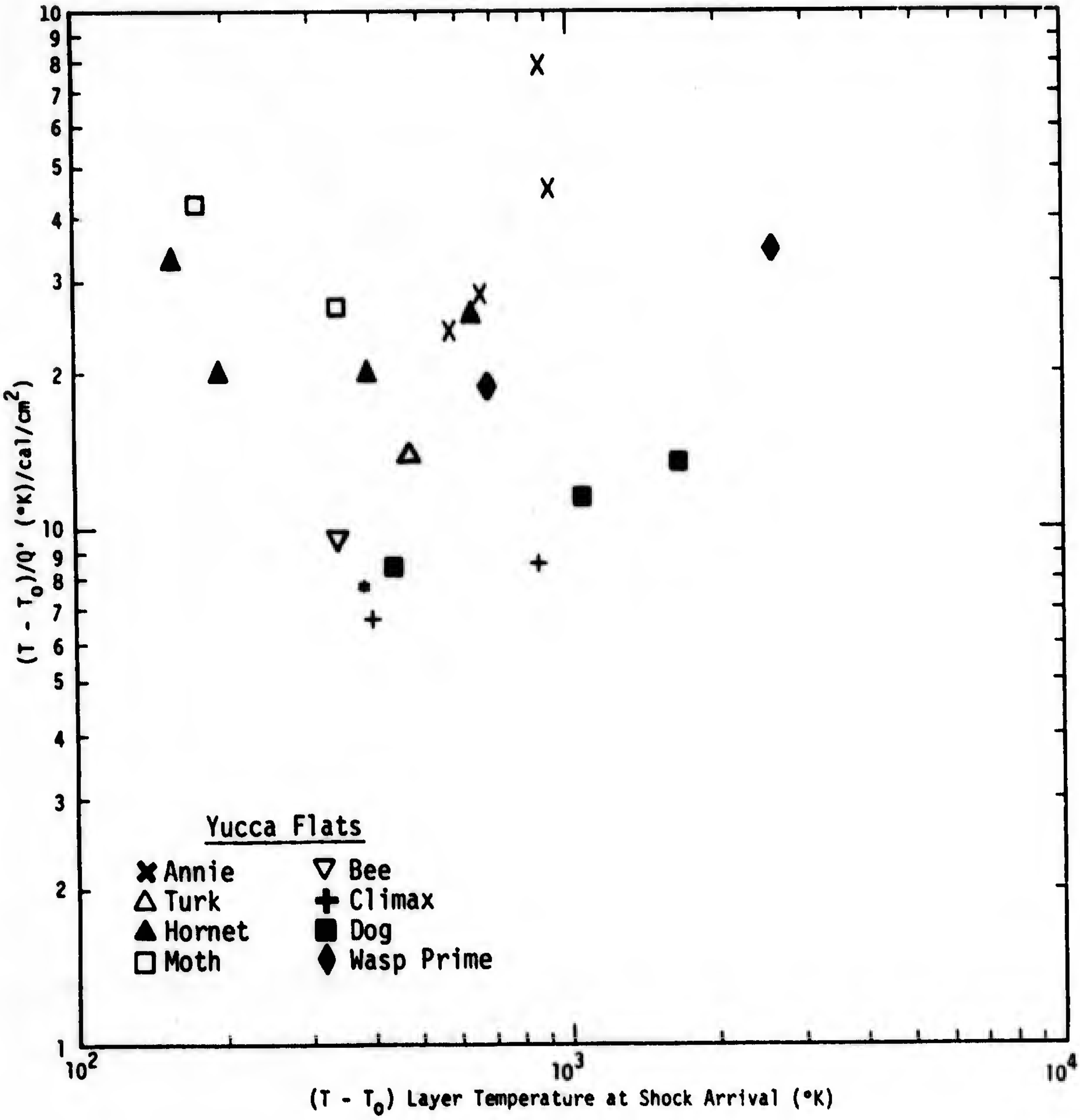

Figure 10a. Layer Normalized Temperature Rise (inverse entropy) Versus Layer Temperature Rise for 12 NTS Atmospheric Test Shots (Yucca Flats Data)

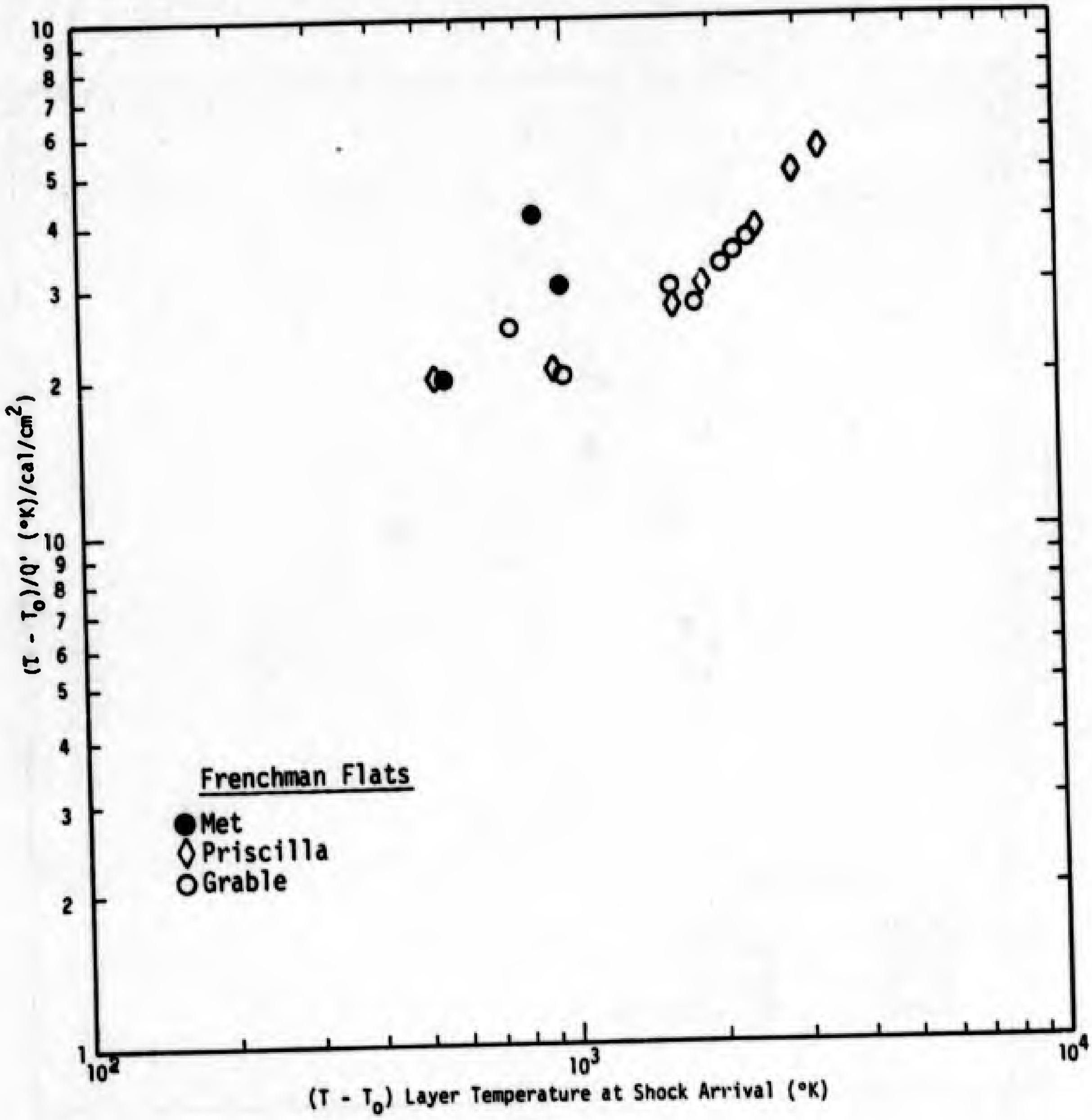

Figure 10b. Layer Normalized Temperature Rise (inverse entropy) Versus Layer Temperature Rise for 12 NTS Atmospheric Test Shots (Frenchman's Flats Data)

7) The systematic trend of

$$\frac{T - T_e}{Q'} \approx \left(\frac{1}{Q'}\right)^{2/3}$$

is observed. The implication is that as the layer temperature rises, it becomes progressively harder to heat. This can, in turn, be attributed to a reduction in layer entropy at higher tempèratures.

8) The solar furnace data on NTS soils at low Q' agree well with the NTS shot values.

Concerning Figure 9:

9) Little conclusive evidence of the dependency of layer temperature on flux has been available up until now. Figure 9 indicates a slow $(Q^{1/2})$ rise in layer heating for the same fluence. Solar furnace test data at lower flux do not corroberate this trend, however.

Concerning Figure 10:

10) A slight dependency on final layer temperature is noted, the rule

$$\frac{T - T_0}{Q'} \sim (T - T_0)^{1/2}$$

can be deduced from these data. Higher final temperatures are reached when the rate of rise is more favorable or higher temperatures lead to lower entropy as noted previously.

11) The solar furnace data point provides excellent confirmation of the results from shock analysis.

In summary, by using a relationship for a normal shock transversing a thermal layer, assuming isentropic conditions, a perfect gas law, and constant γ, we derived general formulae for thermal layer average temperatures as a function of only HOB and yield which agree closely with values measured during the specific shot studied. Analysis of the layer temperature versus radiant heating variables shows generally good agreement with solar furnace test results. The question of flux dependency is not fully resolved. It appears that a slight upward trend of layer temperature rise with flux may be occurring. It may result from layer entropy decreasing at higher heating rates due to the more violent decomposition taking place. Tables 11 and 12 relate the high points of the method and provide a summary for thermal layer temperature analysis.

Table 11. METHOD

- ASSUME FIRST LAW OF THERMODYNAMICS, ISENTROPIC SHOCK FORMATION, PERFECT GAS WITH CONSTANT γ, AND THE CONSERVATION OF LINEAR MOMENTUM TO YIELD

$$M_p^2 = \frac{\gamma + 1}{2\gamma} \frac{\Delta p}{P_o} + 1$$

$$T = \frac{vp^2}{\gamma R M_p^{2}}$$

- IMPLICATION THAT SHOCK IS NORMAL TO GROUND AT BOTTOM OF THERMAL LAYER IS VERIFIED BY GOOD AGREEMENT WITH DATA — WT REPORTS USED SHOCK ANGLE <u>ABOVE</u> THE THERMAL LAYER

- COMPARISON OF METHOD VERSUS DATA ON SHOT PRISCILLA CONSISTENT

- FITTING $v_p = f$ (HOB, W, GR, t) FOR ALL NTS SHOTS YIELDS A UNIVERSAL T IF Δp IS KNOWN

- COMPARISON OF T WITH Q AND $\dot{Q}$ VALUES MAY SHOW TRENDS WITH PHYSICAL IMPLICATIONS.

Table 12. SUMMARY

- A CONSISTENT METHOD FOR PREDICTING Tp FOR NTS SOILS HAS BEEN ESTABLISHED FROM 12 KEY TEST RECORDS
- THE ROLE OF MOISTURE IS UNDERSTOOD AND CAN BE PARAMETRICALLY HANDLED
- THE BACKED OUT TEMPERATURES CAN BE USED TO CALIBRATE MORE ADVANCED MODELS, AND REPRESENT THE ONLY DATA AT HIGH FLUXES NOW AVAILABLE
- EMPIRICAL DATA SCALING WITH Q' AND $\dot{Q}$ HAVE BEEN ESTABLISHED.

Section 3

CALCULATION OF THERMAL LAYER DEVELOPMENT FOR ARBITRARY INITIAL CONDITIONS

3.1 INTRODUCTION

As part of DNA-supported research in determining effects resulting from nuclear burst precursors. SAI has developed a computerized model for determining the thermal layer characteristics that provide the driving forces for the precursor wave. This model is the result of a combination of theoretical analyses and experimental work. The model, which has been named DUSLAR, computes temperature distributions in the air near the ground surface resulting from the interaction of thermal radiation with reactive soils. The variety of physical processes that occur during the blowoff process have been modeled by differential and algebraic equations. These equations are solved simultaneously to obtain the appropriate response functions for the precursor model. The DUSLAR model is primarily aimed at computing temperature profiles near the ground surface and the dust mass distribution in the air, both as a function of time.

The thermal layer model is restricted to processes that occur above soils. Hence, layers developed over vegetation, asphalt, and active surfaces other than soils cannot be treated directly by the present model. Furthermore, it is a one-dimensional model, that is, only variations in a single space dimension, height above the soil surface, are described. This one-dimensional approximation reduces the complexity of the problem and corresponds to the average conditions of thermal layer development.

Briefly, the model operates as follows: First, the incident thermal radiation history from a nuclear burst is determined at the range of interest. The onset of blowoff is determined from empirical relationships. The soil and air heating to the time of blowoff is determined from a thermal conduction model. Puffs of particles (the mass and size distribution given by data) are ejected from the soil and cause heating of the air, with consequent expansion. The air motion tends to keep the particles aloft which then shield underlying soil layers.

The brief outline of the method is described in detail in the next sections. Section 3.2 provides a discussion of general characteristics of the blowoff process. A detailed mathematical description of the various phases of the blowoff process is given in Section 3.3. Section 3.4 describes the computer program and some sample results, while Section 3.5 provides some general observations.

3.2 SOIL BLOWOFF CONSIDERATIONS

The blowoff process and the subsequent formation of the dust layer is a very complex phenomenon. Attempting to model such a process necessarily involves making assumptions. The physical aspects of the thermal layer development, as modeled by the DUSLAR program, are generally based on observations and test data taken with various soils in the White Sands Missile Range (WSMR) Solar Furnace (References 3 and 10). This section describes some general aspects of the problem.

Blowoff of dust from the ground surface due to intense thermal radiation is a complex phenomenon, especially when it involves predicting threshold levels and the blowoff rates. To evaluate such conditions requires a detailed knowledge and understanding of soils with respect to composition and chemical and mechanical behavior. Since soils can exist in a wide variety of compositions and conditions, it is virtually impossible to quantify the phenomena in an analytic sense. One has to resort to experimental data to obtain the necessary information about specific soil types of interest. SAI has done considerable experimentation to identify physical processes and thresholds at which blowoff is initiated. Results of these experiments are described in References 3 and 10. A considerable body of information exists about the behavior of soils, and clays in particular, as exemplified by Reference 11. The following paragraphs summarize information given in this reference to provide a qualitative insight into the physical aspects of soil and soil components at elevated temperatures.

When clays are heated, the following reactions may take place:

1) Loss of hygroscopic and hydrate water
2) Decomposition reactions:
    - Loss of combined water
    - Decomposition of the oxy-salts
    - Oxidation processes
    - Reduction processes
3) Reforming reactions:
    - Recrystallization
    - Recombination
4) Liquid formation
5) Changes on cooling.

The degree to which these reactions occur depends on the nature of the clay and the extent of the heating process. Of particular interest to the present problem is Item 1 above, since it has been postulated as the mechanism for surface dust blowoff.

The loss of hygroscopic water is usually complete at a temperature of 100 to 150°C. The amount to be liberated depends largely on the fineness of the grain size of the minerals in the clay, because the moisture is associated with the surface area of the clay particles. The adsorbed water layer is a variable property ranging from 7.5 to 60 Å in thickness and in all probability a definite limit cannot be ascribed because there is a gradual transition from this form to the normal liquid form. The amount of hygroscopic water retained by a clay is also a function of the humidity of the atmosphere.

Hydrate water is defined as the water of crystallization associated with salts and cations contained in the clay. The temperature at which it is removed is variable, and there can be no sharp distinction between this form and the true combined water of typical clay minerals.

Many of the minerals associated with clays contain water as an inherent part of their structure. As the temperature is progressively raised, such minerals decompose at specific temperatures with the evolution of water. The amount of water lost by each mineral depends on its crystal structure and the number of hydroxyl units contained in the lattice. Table 13 shows the theoretical amounts held in some typical hydrous clays and includes the temperature at which water is given off at a rapid rate. When such minerals decompose with the evolution of water, the solid products which remain are virtually an intimate mixture of the component oxides. The internal arrangement still has many of the characteristics of the original mineral and can be rehydrated to some extent, but oxide components have separate chemical entities.

Because of the large energy depositions that may be encountered in thermal blowoff situations, the melting and vaporization characteristics of clays will be important factors. Liquid formation in clays begins at the temperature of the lowest eutectic point of the components in the mixture; then, with progressively increasing temperature, the amount of liquid phase increases rapidly. In most ceramic materials, little glass is produced below a temperature of 1000°C, unless a considerable amount of alkali is present. Thus, when heated, ceramic materials soften and melt over a wide temperature range and it is usually incorrect to ascribe a particular value as being their

Table 13. THE DECOMPOSITION TEMPERATURES OF SOME CLAY MINERALS

Mineral	Chemical Formula	Temperature of Rapid Decomposition	Percentage Water Lost
Kaolinite	$Al_2O_3 \cdot 2SiO_2 \cdot 2H_2O$	585°C	14.1
Halloysite	$Al_2O_3 \cdot 2SiO_2 \cdot 2H_2O$	558°C	14.1
Montmorillonite	$Al_2O_3 \cdot 4SiO_2 \cdot h_2O$ (ideal)	678°C	5.0
Muscovite Mica	$K_2O \cdot 3Al_2O_3 \cdot 6SiO_2 \cdot 2H_2O$ (ideal)	856°C	4.5
Hydrous Mica	As above but less alkali and more water	550°C (upwards)	6.0 - 10.0
Gibbsite	$Al(OH)_3$	325°C	34.6
Goethite	$FeO(OH)$	350°C	10.1

melting point. The change of ceramic materials into vapors is seldom regarded as a simple physical change. It is usually one result of chemical decomposition such as the reduction of silica to silicon monoxide or silicon which are readily volatized at high temperatures, but are soon reoxidized and deposited as a white powder.

The DUSLAR dust layer model is based on the authors' interpretation of the available experimental data as described in References 3 and 10 and high-speed and low-speed movies of various test runs. The description given below forms the basis of the mathematical models incorporated in DUSLAR.

The process of the development of the thermal layer over soils is broken down into two distinct phases, the pre-blowoff heating phase and the post-blowoff phase. During the first phase the incident thermal radiation serves to raise the soil to increasingly higher temperatures. This causes heating and vaporization of the loosely bound waterforms in the soil, the burning of organic materials with low ignition points, and the decomposition of weakly bonded organics. These processes are generally evident by the formation of smoke immediately above the soil surface. It should be noted that soil is not fully compacted and that pores and small interstitial spaces in the soil grains exist and contain water that cannot readily escape to the atmosphere. The result is vaporization of the water and the resulting buildup of pressure in the interstitial spaces. A violent eruption, or blowoff, results once the forces that provide the bonding between grains and particles are overcome. These eruptions do not occur uniformly over the surface but are a great number of individual events from randomly spaced locations, like miniature erupting volcanos. This has been observed in the high-speed movies discussed above. The events are schematically diagramed in Figure 11. Once blowoff has been initiated, the second phase is in operation. For a short period after the inception of blowoff, continued irradiation causes the additional release of soil puffs. Each puff of particles is

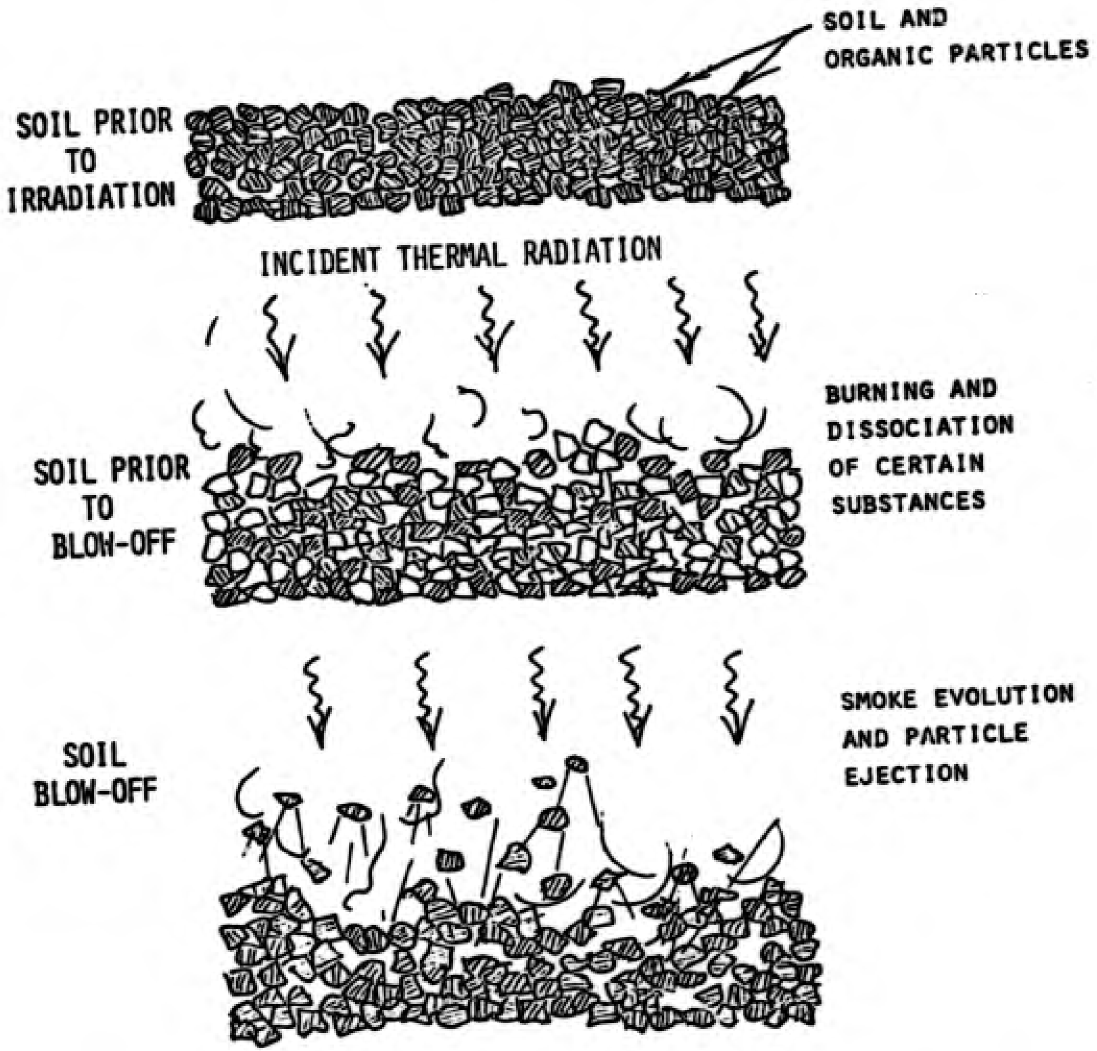

Figure 11. A Schematic of the Thermal Blowoff Process

initially quite hot when it is released by the soil but is cooled by the air into which it is ejected. However, during this period of travel, the ejected particles continue to be heated by the incoming radiation and hence may increase their temperature as the result from this absorption process. The energy transferred from the particle to the air occurs primarily by convection. In a large mass of particles, such as found under blowoff conditions, the effects of radiation are accounted for by the volumetric attenuation of the radiation in the layer. The energy deposited in the air causes it to expand and hence to attain an upward velocity. This upward velocity will tend to drag the dust particles upward, thickening the dust layer. As the dust layer grows and additional soil puffs are liberated in the air, the soil surface underneath the dust layer may become obscured to the thermal radiation. The release rate of blowoff dust decreases gradually until finally the blowoff process ceases. Depending on the thermal radiation history, the thermal layer may still grow after cessation of blowoff.

The considerations given above show the complexity of modeling the thermal blowoff phenomena accurately. It is inherently not possible to treat the phenomena in detail. The model will thus necessarily be an oversimplification of the processes that take place but, hopefully, the important parameters have been included. The next sections provide details on how the various individual processes are modeled and how they all fit together to simulate the development of the thermal layer.

3.3 MATHEMATICAL MODEL

3.3.1 General Aspects

The previous sections discussed the qualitative aspects of the physical processes of the blowoff process and the subsequent development of the thermal layer. The following sections describe how these phenomenologies are represented by mathematical relationships. In general, these relationships are in the form of differential equations and algebraic equations that cannot be solved in closed form. The model equations are hence solved numerically on a digital computer. Figure 12 shows schematically the various events in the model. As described earlier, the development of the thermal layer can be thought of as consisting of two problems, the pre-blowoff heating period and the post-blowoff dust generation period. The first period is modeled strictly as a heat conduction problem in both the soil and air, and the partial differential equation describing it is solved numerically. Pressure perturbations are not affected by it. The second period is modeled by a series of puffs of particles of different sizes that are released from the ground surface. The thermal radiation impinges on top of the dust layer, which is formed by these puffs, through which it subsequently penetrates to the ground surface when the dust density in the air is not too large. Attenuation occurs in the dusty air, the thermal radiation being converted to internal energy in the dust particles. The trajectories of the various puffs are evaluated taking into account the relative velocities between the air and the particles. The dust particles heat up, transferring part of their energy to the air which expands and tends to drag the particles. The differential equations that describe all of these processes are solved numerically and in some instances iteratively. In the following sections, these equations are given along with the iterative procedures for solution.

3.3.2 Pre-Blowoff Heating

Prior to the initiation of blowoff, the soil and the adjacent air layers are heated by the incident thermal radiation. This heating process is assumed to occur strictly by conduction. The basis for this assumption is that the timeframe prior to blowoff is very short, fractions of a second, during which forced and natural connection phenomena can exert little influence. In addition, experimental

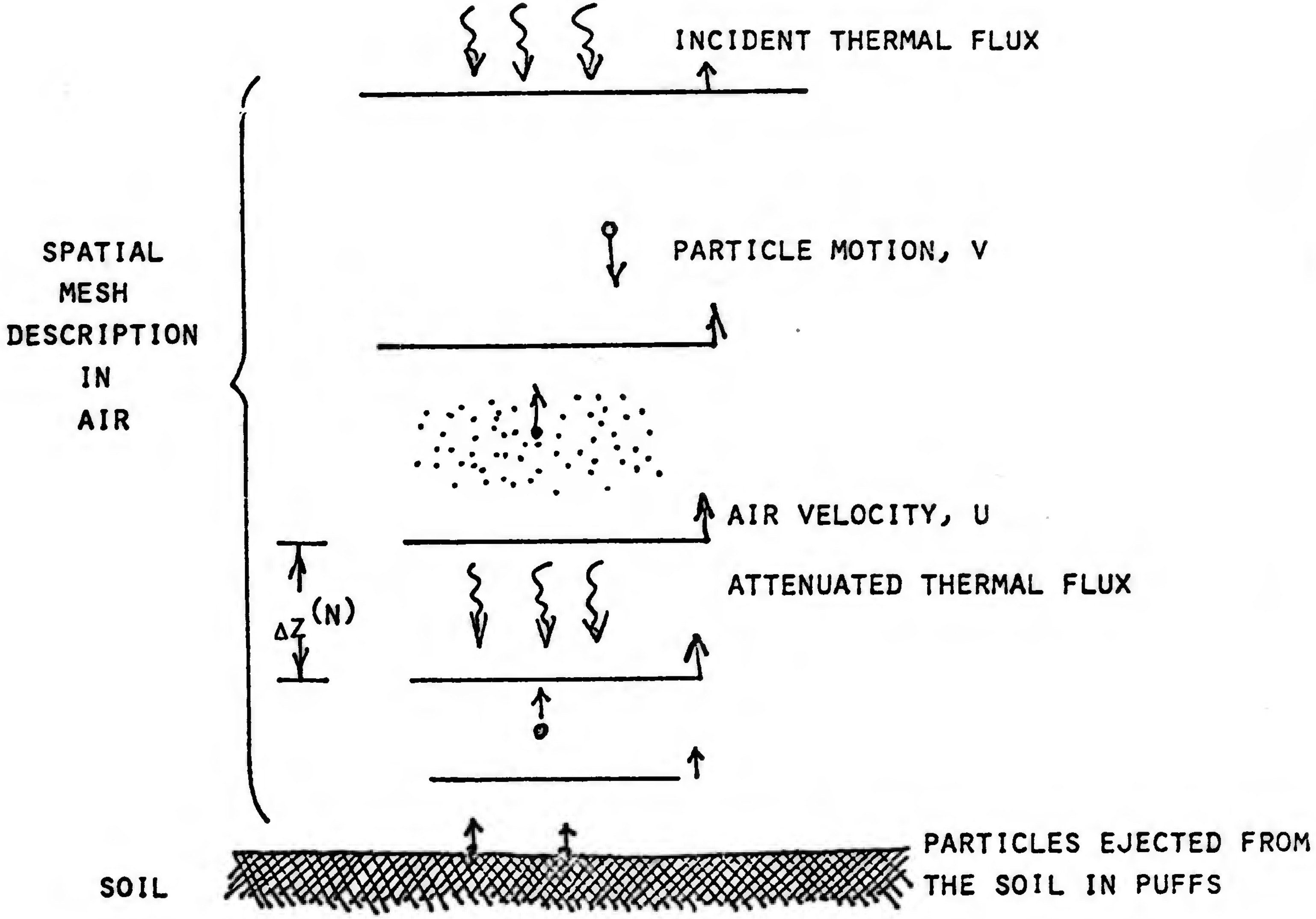

Figure 12. A Schematic of the Model

evidence (Reference 10) shows that this indeed is the case. During the pre-blowoff period, the soil is assumed to be diathermanous, i.e., it is semitransparent to radiation and, as such, absorbs the radiant heat arriving at the surface over a range of depths. The energy flux can then be approximated by:

$$q''(z) = a''(o)e^{-\mu z} \tag{1}$$

Here q"(1) is the radiation flux at the surface and μ is the absorption coefficient. Note that for an opaque solid $\mu \to \infty$, and all radiation energy is absorbed at the surface $z = 0$ and then conducted inward. The one-dimensional heat conduction equation used during the pre-blowoff period is:

$$\rho C_p \frac{\partial T}{\partial t} = \frac{\delta}{\delta z}\left(k \frac{\delta T}{\delta z}\right) + S \tag{2}$$

$$\text{where} \quad S = \frac{dq''}{dz}$$

This equation is highly nonlinear and not readily amenable to an analytic solution for the given set of parameters. That is, the fact that two materials, soil and air, are involved, one of which has properties that vary strongly as a function of temperature, and that the heat source term is both time- and space-dependent, dictates that a numerical solution technique be employed. For both simplicity and accuracy, a fully implicit procedure has been chosen. The finite difference equations given below relate to the geometry description shown in Figure 13. First the relationships are given for the nodes in air for which the source term is zero. Denoting with a prime the new temperatures, the basic finite difference equation is given by

$$(\rho C_p)_j \frac{T'_j - T_j}{\Delta t} = \frac{k_j^+ \frac{T'_{j+1} - T_j}{\Delta z_j^+} - k_j^- \frac{T'_j - T_{j-1}}{\Delta z_j^-}}{\frac{1}{2}(\Delta z_j^+ + \Delta z_j^-)} + S_j \qquad (3)$$

where

$$\Delta z_j^+ = \frac{1}{2}(\Delta z_j + \Delta z_{j+1})$$

$$\Delta z_j^- = \frac{1}{2}(\Delta z_j + \Delta z_{j-1}).$$

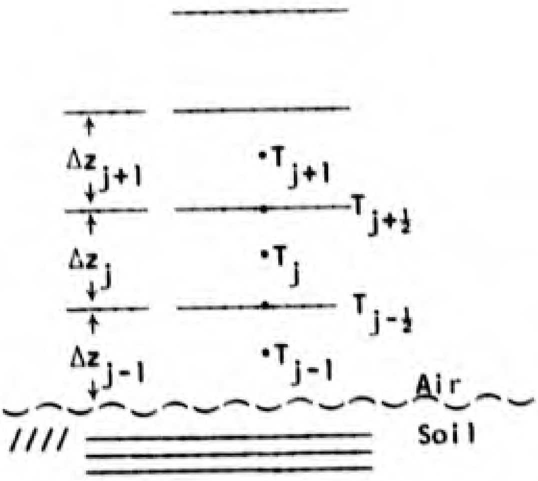

Figure 13. The Spatial Grid Nomenclature for the Conduction Model

The k_j^+ and k_j^- thermal conductivities are determined from an energy balance from node j to j + 1 and j to j - 1, respectively, i.e.,

$$k_j \frac{T_j - T_{j+1/2}}{\frac{1}{2}\Delta z_j} = k_{j+1} \frac{T_{j+1/2} - T_{j+1}}{\frac{1}{2}\Delta z_{j+1}} = k_j^+ \frac{T_j - T_{j+1}}{\Delta z^+} \qquad (4)$$

By solving the first two for $T_{j+1/2}$ and substituting in the last two and some manipulation, one gets

$$\frac{k_j^+}{\Delta z_j^+} = \frac{2}{\dfrac{\Delta z_{j+1}}{k_{j+1}} + \dfrac{\Delta z_j}{k_j}} \quad . \tag{5}$$

Similarly for k_j^-

$$k_{j-1} \frac{T_{j-1} - T_{j-1/2}}{\frac{1}{2}\Delta z_{j-1}} = k_j \frac{T_{j-1/2} - T_j}{\frac{1}{2}\Delta z_j} = k_j^- \frac{T_{j-1} - T_j}{\Delta z_j^-}$$

$$\frac{k_j^-}{\Delta z_j^-} = \frac{2}{\dfrac{\Delta z_j}{k_j} + \dfrac{\Delta z_{j-1}}{k_{j-1}}} \quad . \tag{6}$$

Note that for equally spaced intervals, $\Delta z_j = \Delta z_{j+1} = \Delta z_{j-1} = \Delta z$, and constant thermal conductivity, $k_j = k_{j-1} = k_{j+1} = k$ the difference equation, Equation 3, reduces to

$$(\rho C_p)_j \frac{T_j' - T_j}{\Delta t} = \frac{k}{\Delta z^2} = \frac{k}{\Delta z^2}(T_{j+1}' - 2\,T_j' + T_j') + S_j \tag{7}$$

which is the form usually given.

The new temperatures, T', are found by solving the system of equations given by

$$A_j\,T_{j-1}' + B_j\,T_j' + C_j\,T_{j-1}' = D_j \tag{8}$$

where

$$A_j = -\frac{k_j^-}{\Delta z_j^-}\,\frac{1}{\frac{1}{2}(\Delta z_j^+ + \Delta z_j^-)}$$

$$B_j = \frac{(\rho C_p)_j}{\Delta t} + \frac{1}{\frac{1}{2}(\Delta z_j^+ + \Delta z_j^-)}\left[\frac{k_j^+}{\Delta z_j^+} + \frac{k_j^-}{\Delta z_j^-}\right]$$

$$C_j = -\frac{k_j^+}{\Delta z_j^+}\,\frac{1}{\frac{1}{2}(\Delta z_j^+ + \Delta z_j^-)}$$

$$D_j = S_j + \frac{(\rho C_p)_j}{\Delta t}\,T_j\ .$$

The one-dimensional conduction process as defined for the DUSLAR problem is basically one for an infinite two-material space. Since only a finite number of nodes can be carried in the calculations, boundary conditions at finite distances from the two-material interface have to be specified. Two options are provided in DUSLAR; an adiabatic boundary and a constant-temperature boundary. Consider first the adiabatic condition. If the last node is J, then an adiabatic surface at J + 1/2 is defined such that $T_{J+1} = T_J$. By substituting this condition into Equation 8, then the coefficients are found to be

$$A_J = -\frac{k_J^-}{\Delta z_J^-}\,\frac{1}{\tilde{\Delta z}_J}$$

$$B_J = \frac{(\rho C_p)_J}{\Delta t} + \frac{k_J^-}{\Delta z_J^-}\,\frac{1}{\tilde{\Delta z}_J}$$

$$C_J = 0 \qquad (9)$$

$$D_J = S_J + \frac{(\rho C_p)_J}{\Delta t} T_J$$

$$\tilde{\Delta z}_J = \Delta z_J + \frac{1}{2} (\Delta z_J + \Delta z_{J-1}) .$$

Similarly, for an adiabatic condition at the other end, for j = 1, one gets

$$\begin{aligned}
A_1 &= 0 \\
B_1 &= \frac{(\rho C_p)_1}{\Delta t} + \frac{k_1^+}{\Delta z_1^+} \frac{1}{\approx{\Delta z}_1} \\
C_1 &= - \frac{k_1^+}{\Delta z_1^+} \frac{1}{\approx{\Delta z}_1} \qquad (10) \\
D_1 &= S + \frac{(\rho C_p)_1}{\Delta t} T_1 \\
\approx{\Delta z}_1 &= \Delta z_1 + \frac{1}{2} (\Delta z_1 + \Delta z_2) .
\end{aligned}$$

If, however, temperatures are given as the boundary conditions, then these temperatures are to be substituted into Equation 8 for T_{J+1} in the J^{th} equation and letting Δz_{J+1} go to zero. With some manipulations, the coefficients are easily derived. Similarly, at the other end, for the first equation, the specified temperature is substituted for T_{-1} and letting Δz_{-1} go to zero.

The source term S_j is zero for the air nodes, and given by Equation 11 for the soil nodes in finite difference form.

$$S_j = \frac{q''_{j+\frac{1}{2}} [1 - \exp (- \mu \Delta z_j)]}{\Delta z_j} . \qquad (11)$$

The solution procedure for the set of equations defined by Equation 8 is given in Appendix A.

3.3.3 The Fireball Thermal Radiation Model

The thermal radiation model included in DUSLAR is based on an air burst model consisting of empirical yield scaling laws for the fireball parameters and an empirical representation of the thermal pulse shape. The development of this model has been documented in detail in References 12 and 13. The essential features of the model are summarized in this section.

The fireball for airbursts is represented as follows.

For the time prior to the first minimum, t_1, the fireball radius is taken to be constant and equal to the radius at first minimum, R_1. For the time following the second maximum, t_2, the fireball radius is taken to be constant and equal to its value at second maximum, R_2. For the time interval between t_1 and t_2, the fireball radius, R_f, is represented by:

$$R_f = R_2 \left(\frac{t}{t_2}\right)^{\alpha} \qquad (t_1 < t < t_2) \tag{12}$$

where

$$\alpha = \frac{\ln (R_2/R_1)}{\ln (t_2/t_1)}$$

Yield dependence is determined by scaling laws of the form given by Equation 13.

$$
\begin{aligned}
R_1 &= R_{1o}W^{.36} \\
R_2 &= R_{2o}W^{.39} \\
t_1 &= t_{1o}W^{.5} \\
t_2 &= t_{2o}W^{.44}
\end{aligned}
\tag{13}
$$

The thermal pulse shape is specified in the form

$$P/P_{max} = F\ (t/t_{max}). \tag{14}$$

$F(t/t_{max})$ is taken to be a universal function (i.e., independent of yield) and has the properties $F(0) = 0$, $F(1) = 1$, and $\dot{F}(1) = 0$.

The source for the air burst model is given by Equation 15.

$$S(t) = \frac{P_{max}}{4\ \pi R_f^{\ 2}} F\ (t/t_{max})\ . \tag{15}$$

The normal flux of thermal radiation at the ground surface, $J(r,t)$, at ground range r and time t is given by Equation 16, where $S(t)$ is the power emission rate of the fireball per unit surface area, as given by Equation 15.

$$J(r,t) = S(t)\ k(\rho,\sigma) \tag{16}$$

at time t, $\rho = r/R_f$, $\sigma = h/R_f$, and h is the height of burst. The function $k(\rho,\sigma)$ is referred to as the "fireball shape factor" and is the fraction of the above-ground portion of the fireball radiating normal to the ground surface. The model includes the time dependence of the fireball height as it is affected by buoyancy, gravity, and drag forces. For the case of a near-surface burst, when the fireball intersects the ground surface, an effective yield is defined to simulate the fact that, in this case, most of the energy incident upon the ground is reradiated back into the fireball.

3.3.4 The Blowoff Threshold

The point at which the first soil particles are ejected into the air is defined as the blowoff threshold. This may be past the time at which smoke starts to evolve from the surface. Based on the experimental data given in Reference 10, the threshold level is defined in terms of fluence. For Frenchman's Flat type soils, for which the soil characteristics are reasonably well known, the threshold fluence is given by

$$Q_{th} = 6.5 \text{ cal/cm}^2 \tag{17}$$

This value applies to dry soil only.

3.3.5 The Soil Blowoff Rate

The soil blowoff rate is expressed by an empirical relationship for Frenchman's Flat type soils, which is based on data from Reference 10. The dust generation process is approximated by the relation

$$\frac{\Delta W}{\Delta Q'} \equiv \frac{\text{weight loss of sample}}{\text{fluence beyond threshold}} \simeq 0.00065 \text{ gm/cal.} \tag{18}$$

As given here, the weight loss includes water, combustion products (smoke), and sand particles. However, for dry Frenchman's Flat soil, the weight loss is primarily that of ejected soil particles. Moisture or change to another soil type will affect not only the total value but the mix of evolved particles as well. Equation 18 can be made a differential equation resulting in the following expression:

$$\begin{aligned} \frac{dw}{dt} &= 1.6 \times 10^{-7} \frac{dQ}{dt} && \text{for } Q \geq Q_{th} = 2.7 \times 10^5 \\ \frac{dw}{dt} &= 0 && \text{for } Q < Q_{th} \end{aligned} \tag{19}$$

where the units are expressed in SI (m, kg, sec, Joule, ^{o}K).

The soil mass, W, is assumed to contain particles of different sizes of R, the size distribution of which can be described by the mixed distribution

$$\frac{dW_1}{dx} = C_1 \frac{1}{\sigma\sqrt{2\pi}} \exp\left[-\frac{x - \mu_o}{2\sigma^2}\right] \qquad R < 0.018 \text{ cm}$$

$$\frac{dW_2}{dx} = C_2 \; 10^{0.5x} \qquad R \geq 0.018 \text{ cm}$$

$$x = \log(R)$$

$$\sigma = 0.3 \tag{20}$$

$$\mu_o = x_o + 6.908\sigma^2$$

$$x_o = \log(\bar{R})$$

$$\bar{R} = 0.002$$

$$\left.\begin{aligned} C_1 &= 0.5831 \times 10^{-3}/\text{kg} \\ C_2 &= 1.3591 \times 10^{-3}/\text{kg} \end{aligned}\right) \text{ based on a maximum particle size of 0.1 cm.}$$

The mass lofted in the air is presently classified in four particle size classes, two above the 0.018 cm and two below. The 0.018 cm cutoff is such that approximately half of the total mass falls above it and half below it. Table 14 shows the appropriate number densities that can be derived with the above equations.

3.3.6 The Motion of a Particle

The motion of particles is described by the standard relationship for Newton's second law. The appropriate differential equations are given by Equations 21 and 22 given the velocity and displacement as a function

Table 14. PARTICLE SIZE CLASSES

Class No.	Particle Size (microns)	Number Density* (#/kg)
I	37	3.69×10^6
II	109	1.48×10^5
III	344	4.59×10^3
IV	754	4.34×10^2

---

* Based on a particle density of 2.54 g/cm^3.

$$m_p \frac{dV}{dt} = - F_d - F_g \tag{21}$$

$$\frac{ds}{dt} = V \tag{22}$$

of time. The drag force, F_d, and the gravitational force, F_g, are given by Equations 23 and 24. The drag coefficient, C_d, is discussed in Section 3.3.7.

$$F_d = C_d A_c \frac{\rho a (V-u)|V-u|}{2} \tag{23}$$

$$F_g = mg \tag{24}$$

where

$$m_p = \frac{4}{3} \pi r^3 \rho_p$$

$$A_c = \pi r^2$$

The equations given above apply to each particle size and to each puff. The particle mass is assumed to be constant. The air density necessary to compute the drag force depends only on the air temperature.

3.3.7 The Particle Drag Coefficient

The magnitude of the drag coefficient of particles in dusty atmospheres is difficult to assess due to a great number of factors, some of which will be discussed here briefly. First, the shape of dust particles is generally expected not to be spherical, although this will be assumed for calculational purposes. The effect of shape has been investigated by a number of people, both experimentally and analytically. The general conclusion seems to be that in the Stokes regime; that is, for particle Reynolds numbers less than 1 if the maximum-to-minimum diameter does not exceed 4, the Stokes' law for spheres could be applied with little error using a radius of the sphere that has the same volume. For higher Reynolds numbers, the problem becomes more complicated and the data more diverse. Figure 14, taken from Soo (Reference 14), demonstrates the range of results obtained by various investigators varying from a factor of 3 above the standard drag curve to a factor of 100 below it. Many of the measurements shown in this figure were plagued by inaccuracies of one form or another so that no great faith should be placed in them. The figure merely serves to illustrate the fact that particle drag in dusty flows is not a well known science. Aside from particle shape, there are other factors that influence the motion of particles, such as rotation, fluid shear, thermophoresis, photophoresis, and pressure gradients. These forces are generally expected to be small compared to the drag force.

For the dusty layers subjected to intense radiation and, hence, high temperatures, an effect that is generally not recognized may be quite important, although difficult to model at present because of lack of data. Particles that are burning or evaporating exhibit significant changes in their drag behavior. Figure 15, taken from Cadle (Reference 15), shows how the drag coefficient of evaporating isotane particles varies as a function of Reynolds number. As may be noted, the drag coefficient could be lower by a factor of 10 as compared with the standard drag law for solid spheres. As mentioned above, there are inadequate data available to model the present problem.

The drag coefficient used in the model is a fit to the solid smooth sphere data. The correlation is due to Torobin and Gauvin (Reference 16) and is given by Equation 25.

$$C_d = \frac{24}{Re_p} \left(1 + 0.15\, Re_p^{\,0.687}\right) \tag{25}$$

This correlation is good up to a Reynolds number of 1,000, as noted in Table 15 where the fit is compared with the reference values given by Goldstein (Reference 17).

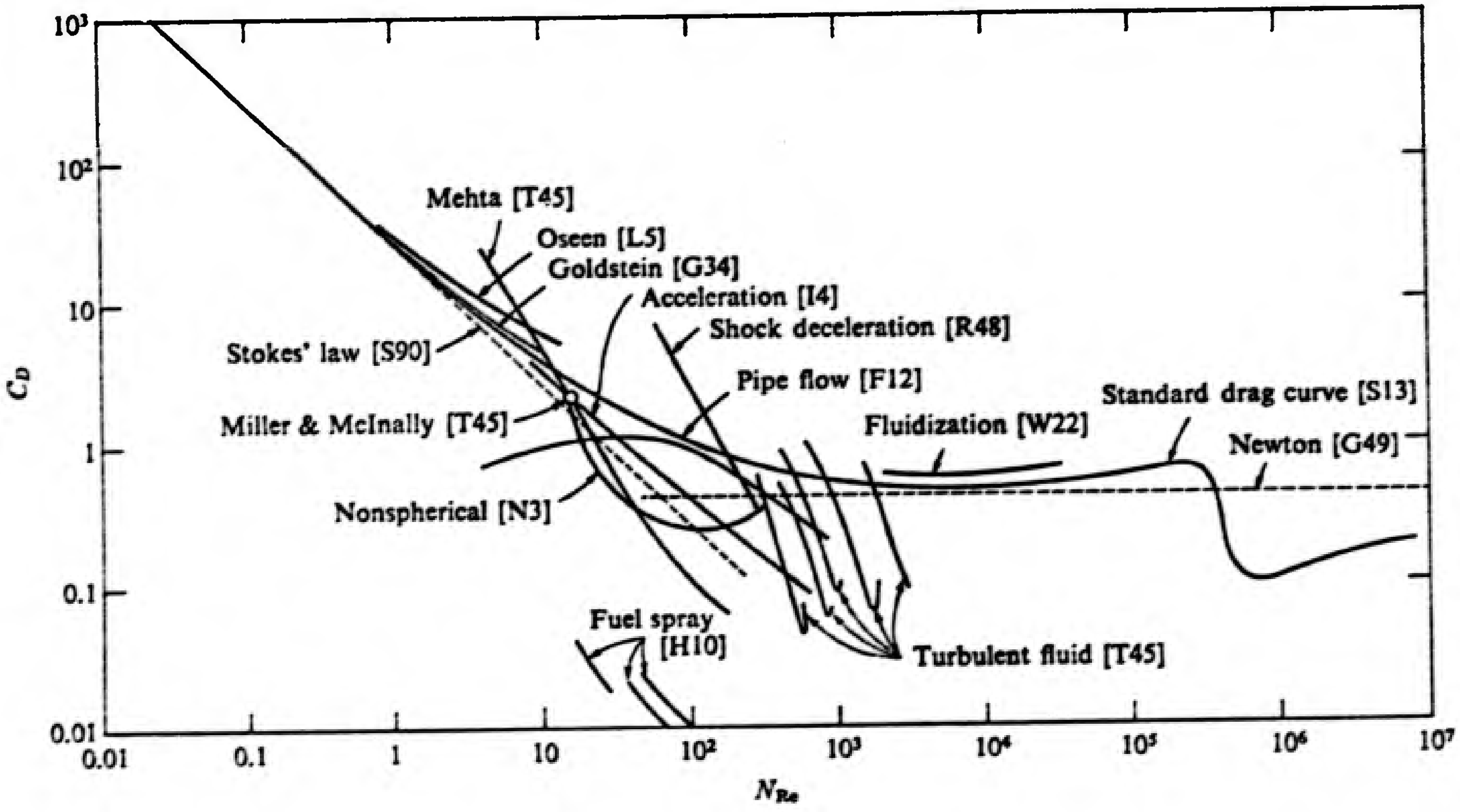

Figure 14. The Drag Coefficient of a Sphere

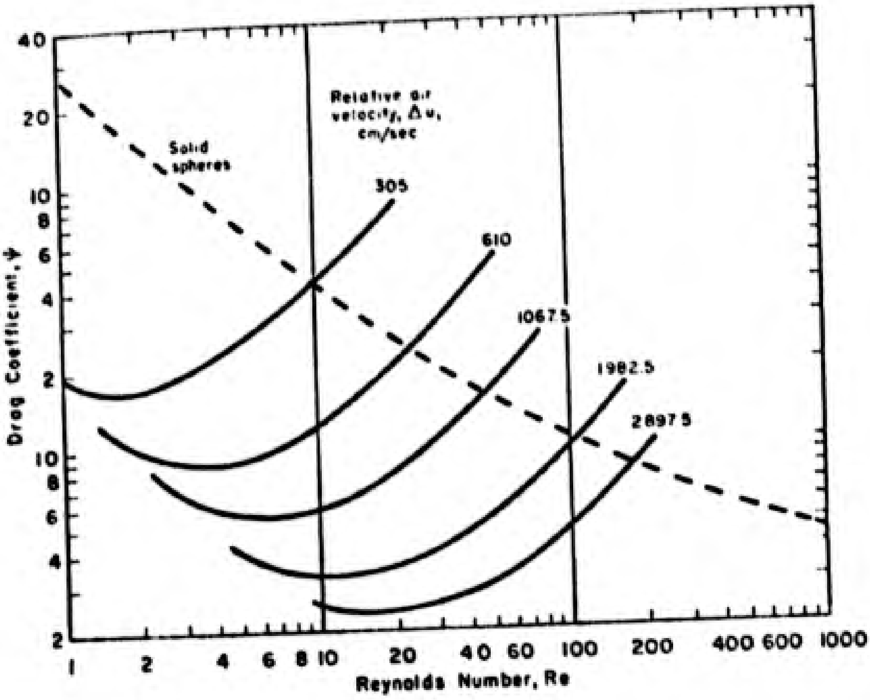

Figure 15. Relation Between Drag Coefficient and Reynolds Number for Isoctane Droplets and Solid Spheres.

Table 15. VALUES OF DRAG COEFFICIENTS

Re	C_d (experimentally, Reference 17)	C_d (correlation, Equation 25)	% difference
.01	2400.	2415.	0.63
.1	244.	247.	1.2
.4	63.	64.	1.6
1.0	26.2	27.6	5.3
4.0	8.20	8.33	1.6
10	4.27	4.15	-2.8
30	2.03	2.05	0.99
60	1.36	1.40	2.9
100	0.05	0.09	3.8
300	0.660	0.684	3.6
600	0.525	0.526	0.19
1000	0.455	0.438	-3.7
2000	0.394	0.345	-12.4

3.3.8 The Heat Transfer from a Particle

The time-dependent heat transfer from particles is based on the thermally thin body or lumped mass approximation. A thin body has insufficient internal thermal resistance to support any significant temperature gradients so that the temperature throughout the body can be assumed uniform. A rough criterion of whether such an assumption is valid is given by Equation 26.

$$Bi = \frac{hr}{k_p} < 0.1 \tag{26}$$

The Biot number, Bi, expresses the ratio of surface-to-internal conductance. This limit does not constitute a strict criterion because it ignores a time effect. More on this can be found in Reference 18. Sample calculations show that this limit cannot be satisfied for sand particles in air. For up to Reynolds numbers of 100, the Biot number varies from approximately 0.2 to 0.4. This variance was not found to be too significant and thus did not warrant a more detailed particle temperature calculation in view of other uncertainties in the present methodology.

The temperature response of a particle is given by Equation 27.

$$mC_p \frac{dT}{dt} = - q_c'' A_p + q_a''' V_p \tag{27}$$

where

$$q_c'' = h\,(T - T_a)$$

$$A_p = 4\,\pi r^2;\; V_p = \frac{4}{3}\pi r^3$$

The volumetric heat generation rate is derived in Section 3.3.10.

The heat transfer rate from particles submerged in a fluid is equally uncertain, as was the case with the drag coefficient discussed in Section 3.3.7. Analytical results exist for a completely quiescent fluid, in which case pure conduction is the mechanism. With relative motion, solutions exist for very low Reynolds numbers, but as the relative velocity increases, variables such as turbulence, variable fluid properties, flow separation, etc., complicate the analysis to the point where reliable expressions can no longer be derived. For higher Reynolds numbers experiments are the only answer. The best fit for a single particle or sphere immersed in an incompressible fluid of infinite extent with small temperature differences is given by Equation 28 (Reference 19).

$$Nu = \frac{h\ 2R}{ka} = 2.0 + 0.6\ Re^{1/2}\ Pr^{1/3} \tag{28}$$

In the absence of other data, this relationship has been used to determine the heat transfer rate from the particle to the air.

3.3.9 The Air Flow Relations

The motion of air as it is affected by changes in internal energy due to the heat exchange process with the dust particles is expressed by the Lagrangian formulations of the conservation equations of mass, momentum, and energy in one space dimension. Two basic assumptions are made: the effect of viscosity is neglected, and the whole blowoff process can be considered an isobaric process. The derivation of the equations is given in this section.

The one-dimensional Eulerian equations describing the conservation of mass, momentum, and energy, as used in DUSLAR, and neglecting the effects of viscosity, are given by Equations 29, 30, and 31, where

$$\frac{d\rho}{dt} + \rho\,\frac{\delta u}{\delta x} = 0 \tag{29}$$

$$\rho\,\frac{du}{dt} + \frac{\delta p}{\delta x} = -\ \rho g \tag{30}$$

$$\rho \frac{dE}{dt} + \frac{\delta(pu)}{\delta x} = -\rho u g + \dot{Q} \tag{31}$$

d/dt is the substantial or Lagrangian time derivative. The derivation of these equations can be found in many texts, for example, Bird, Stewart, and Lightfoot (Reference 19). Equation 29 describes the conservation of mass. Equation 30 is Euler's form of the equation of motion, that is, the effects of viscosity have been neglected. Equation 31 expresses conservation of internal and kinetic energy ($E = I + 1/2\, u^2$), and assumes that the work done by viscous forces can be neglected. If specific volume, V, is used instead of density, the conservation of mass equation can be written as

$$\frac{\delta u}{\delta x} = \frac{1}{V}\frac{dV}{dt} . \tag{32}$$

Expanding E and pu in the energy equation, and subtracting from it the equation of motion results in

$$\rho \frac{dI}{dt} + p \frac{\delta u}{\delta x} = \dot{Q} . \tag{33}$$

Assuming next that air behaves as an ideal gas, the equation of state can be written as

$$p\gamma = (\gamma - 1)\, I . \tag{34}$$

Differentiating the equation of state with respect to time and combining it with Equations 32 and 33 leads to

$$\frac{dI}{dt} = \frac{V}{\gamma}\dot{Q} . \tag{35}$$

Combining this equation with Equation 33 leads to an expression for the velocity

$$\frac{\delta u}{\delta x} = \frac{\gamma - 1}{\gamma p}\dot{Q} . \tag{36}$$

Combining this with Equation 32 gives a relation for specific volume

$$\frac{dV}{dt} = \frac{\gamma - 1}{\gamma p} V\dot{Q} \qquad (37)$$

By using Lagrangian coordinates, the process of advection is accurately described and equally the difference algorithm is simple. A Lagrangian mesh is therefore defined so that each mesh point j, to represent the boundary between cells, moves with the local fluid velocity (Figure 16). Each cell i is defined by the boundary points j.

$$x_j(t') = x_j(t) + \int_t^{t'} u_j(s)\, ds \qquad (38)$$

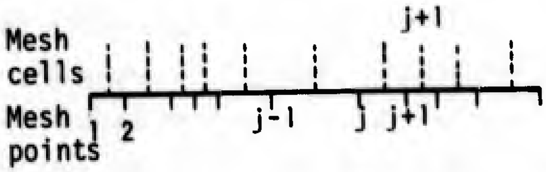

Figure 16. The Lagrangian Mesh in One Dimension

In practice, it is most convenient to define a double mesh. Cell boundaries x_j are defined on the mesh, say $1 \leq j \leq J$, and equally the fluid velocities u_j, equated now with the cell boundary points x_j, are defined on the mesh j. The intensive properties of specific volume and internal energy are defined as cell, rather than point properties and, for this definition, the centers of each cell are defined on a secondary mesh i, $1 < i < I$. Each cell i has width $\Delta_i = x_{j+1} - x_j$. Then the conservation-of-mass equation takes the form:

$$\Delta^n = \frac{V^n}{V^o} \Delta^o \qquad (39)$$

namely, the mass contained in each cell is constant (since the cell boundaries move with the fluid velocity).

Equations 35 and 37 are solved for each cell, after which Equation 39 is used to determine the cell size and Equation 36 to determine the velocity of the cell boundary. In the energy equation, the heat source term $\dot{Q}$ is broken into two components, one due to the heat transfer from the particles to the air and the other due to exchange across adjacent cell boundaries caused by turbulence. Hence,

$$\dot{Q} = S + \frac{k^t}{C_v} \frac{dI}{dz} \tag{40}$$

where k^t could be called a thermal eddy conductivity.

3.3.10 Flux Attenuation in the Dust Layer

After the blowoff process has begun, the dusty layer shields the soil surface to some extent from the incoming thermal radiation. There are various processes that may contribute more or less to the extinction phenomena. The air at this point may not be simply air, but may be augmented by gas by-products of various decompositions that might be going on and a significant increase in water vapor. The attenuation processes in such a particle-loaded gas mixture are not easily quantified. In general (Reference 20), there are three significant mechanisms by which radiant energy interacts with a gas containing particles: 1) absorption by the gas; 2) absorption by the particles suspended in the gas; and 3) scattering by the particles. The importance of each of these three mechanisms depends on the composition, temperature and pressure of the gas; the composition, sizes and shapes of the particles; the particle number density; and the spectrum of the radiant energy.

The attenuation of a beam of monochromatic radiant energy by a gas containing particles is governed by the expression

$$I(\lambda,x) = I(\lambda,o)\, e^{-k_T(\lambda)x} \tag{41}$$

where $k_T(\lambda)$ is the total linear attenuation coefficient for radiant energy of wavelength λ, and x is the distance the beam traverses through the seeded gas. The linear attenuation coefficient for all three interaction processes is equal to the sum of the linear attenuation coefficients for each process separately, that is,

$$k_T(\lambda) = k_a^g(\lambda) + k_a^p(\lambda) + k_s^p(\lambda) \tag{42}$$

where $k_a^g(\lambda)$ is the linear attenuation coefficient due to absorption by the gas alone, $k_a^p(\lambda)$ is the linear attenuation coefficient due to absorption by the particles, and $k_s^p(\lambda)$ is the linear attenuation coefficient due to scattering by the particles. As long as the particles are randomly oriented and the average distance between the particles is much greater than their effective radius, $k_a^p(\lambda)$ and $k_s^p(\lambda)$ are proportional to the number density of the particles.

One may now consider the absorption of radiant energy by particle-seeded gases to be the sum of two independent processes; absorption by the gas itself and absorption due to the particles in the gas. The absorption coefficient of the gas, $k_a^g(\lambda)$, depends only on the composition, temperature, and pressure of the gas; whereas the absorption and scattering parameters of the particles, $k_a^p(\lambda)$ and $k_s^p(\lambda)$, depend on the composition, sizes, and shapes of the particles, Thus, $k_a^g(\lambda)$ may usually be determined for the pure gas and $k_T(\lambda)$ is calculated for the particle-seeded gas using Equation 42. However, this procedure becomes difficult, if not impossible, when the composition of the gas and the sizes and shapes of the particles are changed by chemical reactions between the particles and the gas.

The basic mechanisms of radiant energy absorption by particle clouds and by gases are quite different. Since atoms and molecules of a gas absorb radiant energy in discrete quanta, the absorption coefficient of a gas may change many orders of magnitude over a wavelength interval of a few Angstroms. The familiar absorption spectra of various gases attest to the wide variations of $k_a^g(\lambda)$ as λ is changed.

Whereas gases tend to absorb in lines and bands, the absorption and scattering characteristics of particle clouds vary only gradually with the wavelength of the incident radiant energy. Thus, $k_a^p(\lambda)$ and $k_s^p(\lambda)$ are smoothly varying functions of wavelength. Scattering enhances energy absorption in particle clouds by increasing the average path length traversed by the radiant energy. However, in any given unit volume of aerosol, the particle-gas mixture is heated only by absorption, not by scattering. For this reason, it is convenient to define the absorption coefficient for the dust, $k_a(\lambda)$, by

$$k_a(\lambda) = k_a^g(\lambda) + k_a^p(\lambda) = k_a^g(\lambda) + \rho\, \mu_a(\lambda) \qquad (43)$$

Since the dust layer thickness is very small compared to its lateral extent, any scattering away from a given point is made up by incoming scattered radiation from adjacent regions. Although not strictly true in our present situation, because of the thermal radiation gradient with respect to the ground range, it is thus assumed that scattering can be ignored. The absorption in the gas is another matter. In the present formulation of DUSLAR, it is neglected since no good assumptions could be justified to describe the component gases that would be present. Hence, only absorption in the dust is treated. The discussion above considered the absorption and scattering processes as a function of wavelength. By integrating over the whole wavelength spectrum, one obtains total attenuation. This relationship may be expressed as

$$I(x) = \int_0^\infty I\,(\lambda,o)\, e^{-k_a^T(\lambda)x}\, d\lambda \qquad (44)$$

For an ensemble of particles of differing size, the absorption coefficient is weakly dependent on wavelength. Then this equation may be approximated as

$$I(x) = I_o e^{-k_a^T x} \tag{45}$$

The linear attenuation coefficient due to absorption by the particles is approximated by Equation 46.

$$k_a^p = EA_p \tag{46}$$

where A_p is the true projected area of the particles per unit volume of the dust layer and E is an area efficiency factor. The cross-sectional area per unit volume, A_p, can be calculated from the particle size distribution and the particle concentration as shown by Equation 47.

$$A_p = \sum_i n_i \pi r_i^2 \tag{47}$$

The area efficiency factor, E, can be determined from the formalism of Mie scattering for perfect spheres. For the size of the particles considered here the range of E is from 2.0 to 2.5.

The energy absorbed in the dust layer is assumed to be converted into a uniform volumetric heat source for the particles of strength S. It is expressed by Equation 48.

$$S = \frac{I_o \, [1 - \exp(-k_a^T x)]}{x \cdot \sum_i \frac{4}{3} \pi r_i^3 n_i} \tag{48}$$

where

$$k_a^T = E \sum_i \pi r_i^2 n_i = k_a^g$$

3.3.11 Physical and Thermal Properties

The various properties for soil and air required in the calculations are summarized in this section. For soil, all properties are assumed to be temperature-independent since no reliable data exist to describe them otherwise. For air, the properties are based on simple curve fits to tabulated data from Reference 21. Equations 49 through 62 summarize the relationships presently used. The units are all in SI (m, kg, sec, Joule, °K).

Air density: $\rho_a = \frac{3.487 \times 10^{-3} p}{T}$ (49)

Air kinematic viscosity: $\nu_a = 1.638 \times 10^{-9} T^{1.625}$ (50)

Air thermal conductivity: $k_a = 1.4395 \times 10^{-2} + 4.72108 \times 10^{-5} T$ (51)

Air specific heat: $C_{pa} = 974.0 + 0.1299 T$ (52)

Air ratio of specific heats: $\gamma_a = 1.40$ (53)

Atmospheric pressure: $p_a = 9.80665 \times 10^4$ (54)

Particle density: $\rho_p = 2.54 \times 10^3$ (55)

Particle specific heat: $C_{pp} = 0.85 \times 10^3$ (56)

Soil thermal conductivity: $k_s = 0.276$ (57)

Soil density: $\rho_s = 1.95 \times 10^3$ (58)

Soil specific heat: $C_{ps} = 0.85 \times 10^3$ (59)

Particle melting point: $T_{mp} = 2500°C$ (60)

Particle latent heat of fusion: $H_{sf} = 2.0 \times 10^6$ (61)

Soil absorption mean free path: $\lambda = 0.001$ (62)

3.3.12 Solution Procedure

The various physical processes described in the previous sections are generally in the form of ordinary nonlinear differential equations. The solution method presently used in DUSLAR for solving these simultaneous equations is based on the Runge-Kutta-Merson (RKM) technique. It is basically a fourth-order Runge-Kutta integration procedure, but contains an algorithm to estimate the truncation error after each integration step which is accurate enough for adjusting the time step automatically. There are many other procedures that could have been used, some of which are bound to be more efficient, but the RKM method was found to be both expedient and convenient to use. The formulas for this technique are given by Equation 63.

$$Y_i^{n+1} = Y_i^n + (K1_i + 4 \cdot K4_i + K5_i)/2 + O(h^5) \tag{63}$$

where

$$K1_i = h \cdot F_i(X^n, Y_1^n, Y_2^n, \ldots, Y_{NE}^n)/3$$

$$\begin{aligned} K2_i = {} & h \cdot F_i[X^n + (h/3), Y_1^n + K1_1, Y_2^n + K1_2, \ldots, \\ & Y_{NE}^n + K1_{NE}]/3 \end{aligned}$$

$$\begin{aligned} K3_i = {} & h \cdot F_i[X^n + (h/3), Y_1^n + (k1_1/2) + (K2_1/2), Y_2^n + \\ & (K1_2/2) + (K2_2/2), \ldots Y_{NE}^n + (K1_{NE}/2) + (K2_{NE}/2)]/3 \end{aligned}$$

$$K4_i = h \cdot F_i[X^n + (h/2),\ Y_1^n + (3 \cdot K1_1/8) + (9 \cdot K3_1/8),\ Y_2^n + (3 \cdot K1_2/8) + (9 \cdot K3_2/8),\ .\ .\ .\ .\ ,\ Y_{NE}^n + (3 \cdot K1_{NE}/8) + (9 \cdot K3_{NE}/8)]/3$$

$$K5_i = h \cdot F_i[X^n + h,\ Y_1^n + (3 \cdot K1_1/2) - (9 \cdot K3_1/2) + 6 \cdot K4_1,\ .\ .\ .\ .\ ,\ Y_{NE}^n + (3 \cdot K1_{NE}/2) - (9 \cdot K3_{NE}/2) + 6 \cdot K4_{NE}]/3$$

$O(h^5)$ indicates that the quantity on the right side of Equation 63 provides an approximation to the left side correct to terms of order h^5 as $h \rightarrow 0$. This is not used in the actual calculation.

In the above equations, the subscript i refers to the ith differential equation, the superscript n refers to the previous point just calculated, while n+1 is the point to be calculated.

The advantage of this method is that an estimate of the truncation error, e, is given by

$$e_i = K1_i - (9 \cdot K3_i/2) + 4 \cdot K4_i - (K5_i/2)$$

which is accurate enough for automatic step-size adjustment.

If $MAX(e_i)$ is greater than the pre-assigned accuracy, the interval, h, is halved and the computation for the step is begun again; but if $MAX(e_i)$ is less than 1/32 of the pre-assigned accuracy, the interval is doubled and the calculation for the next step is begun. This method requires five function evaluations per step.

The actual FORTRAN subroutine was taken from Reference 22 and used with some slight modifications.

Section 4

THE DUSLAR COMPUTER PROGRAM

4.1 THE ORGANIZATION OF THE PROGRAM

The DUSLAR computer program solves the equations described in Section 3. The program was developed on a Control Data CYBER 73-18 and test cases were run to completion on a CDC-7600. The DUSLAR system consists basically of two programs, one which solves the equations for the given initial conditions and which writes the results on a results file, and another which processes this results file and prints and plots selected data. The program in its present form is not user oriented since it requires some effort to prepare the input data and to analyze the printed results.

The organization of the program in the various subroutines is shown in Figures 17, 18 and 19. The main program, as shown in Figure 17, calls three subroutines that perform certain basic functions; namely, set constants, initialize variables, and initiate the actual calculations by calling the driver. The initialization process is referred to here as defining the variables just prior to blowoff. Figure 18 shows then what computations are performed at this stage. The routines called by the driver are shown in Figure 19. Again, the functions of the various subroutines are described there. The PROCESS subroutine shown in this figure has also been made a separate program so that it can process the same results file generated during the earlier run and which was saved either on disk or on magnetic tape.

4.2 THE INPUT/OUTPUT DATA REQUIREMENTS

The input data to DUSLAR consists basically of quantities related to the pre-blowoff condition in soil and air, the nuclear burst characteristics, the particle puff characteristics, post-blowoff

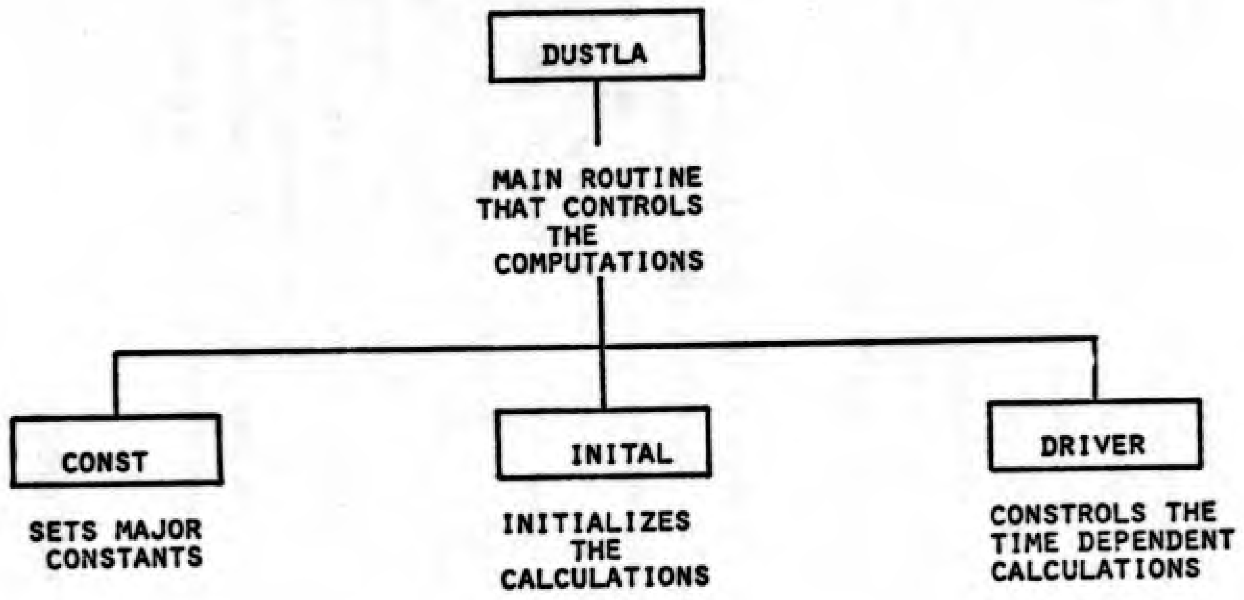

Figure 17. DUSLAR Computer Program Outline

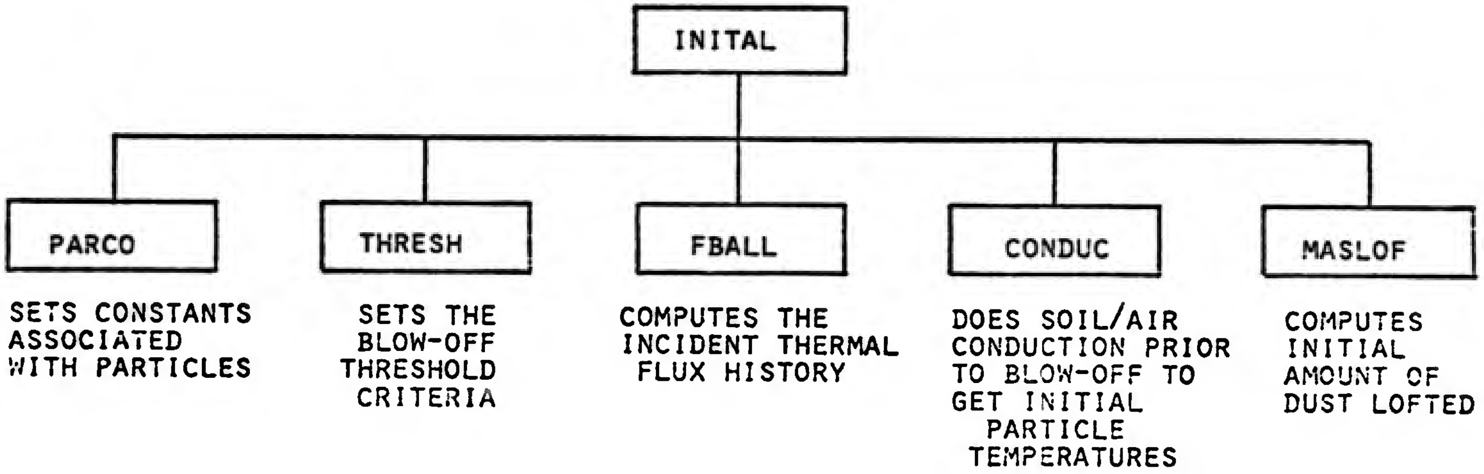

Figure 18. DUSLAR Computer Program Outline (Cont'd)

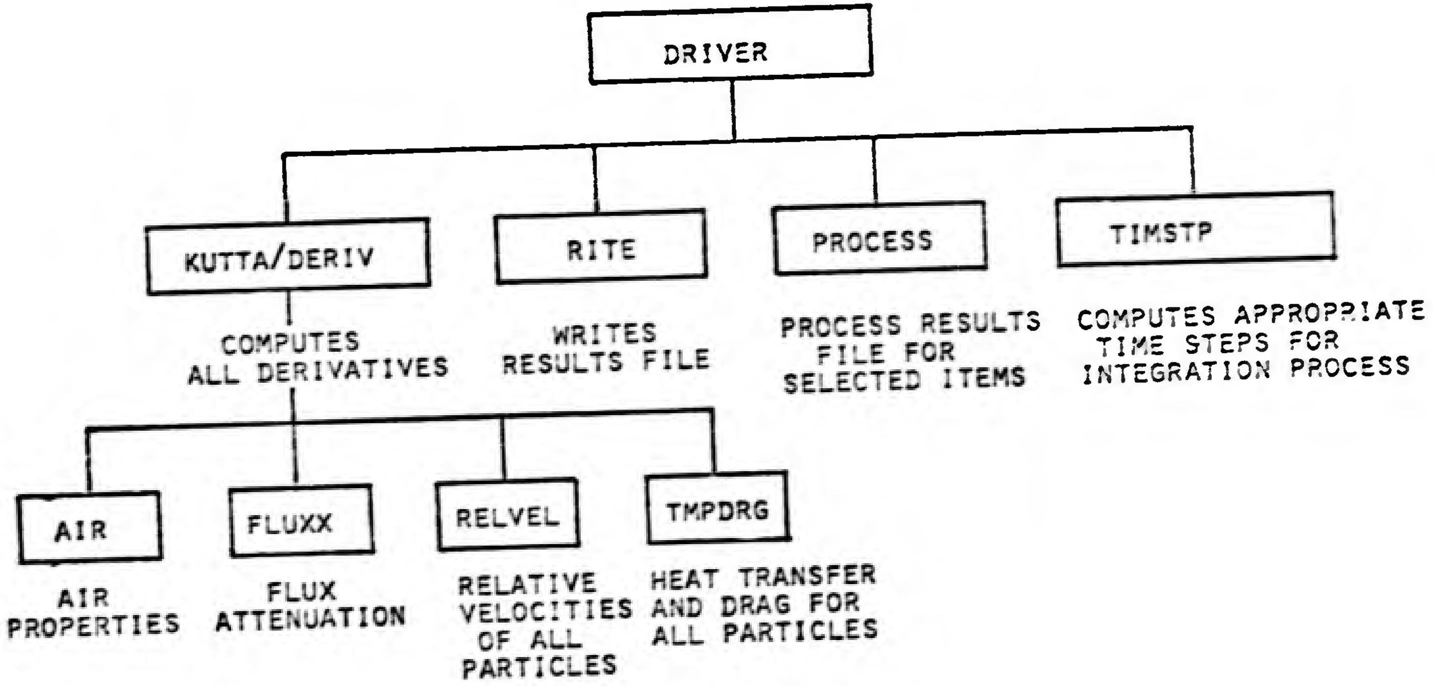

Figure 19. DUSLAR Computer Program Outline (Cont'd)

air parameters, and integration data. Table 16 lists the variables that are presently required as input to DUSLAR and includes sufficient flexibility to investigate the effects of important variables. Their function should be self-explanatory. Data are entered via the NAMELIST feature of CDC FORTRAN IV.

The present limitations of the main variables in the program are tabulated in Table 17. These can easily be changed by altering the appropriate FORTRAN dimension statements.

4.3 PROCESSING THE RESULTS

The results of a calculation are written on Logical Units 7 and 8. The former contains the detailed results of every time step, while the latter contains a few reduced quantities of primary interest. Data on Unit 7 consist of particle trajectory histories, air cell thermodynamic variables and velocities, and dust energy deposition rates. Unit 8 contains the thermal flux histories at the top and bottom of the dust layer, the maximum particle distance from the ground surface and the average dust layer temperature. The data on these files can be processed by the DUSPRO program and presented in table form or, for a select number of items, be graphed by the printer.

4.4 RESULTS OF A CALCULATION

To demonstrate the capabilities of the present version of the DUSLAR program, the calculational results generated to date will be presented. Since the basic objective of this program was to predict dust layer heights and temperatures, it is necessary to define these parameters.

In DUSLAR the dust layer height is defined as the highest location of any dust particle at the given point and time. The thermal layer temperature is defined as the mixed mean temperature of the

Table 16. INPUT DATA REQUIREMENTS FOR DUSLAR

Pre-Blowoff Conduction

NA	Number of spatial intervals in air
NS	Number of spatial intervals in the soil
DXA	Smallest interval size in air
DXS	Smallest interval size in soil
FDXA	Multiplier for air cells to generate remainder of cells
FDXS	Same as FDXA but for soil
AMDA	Characteristic absorption length in soil
TAMP	Initial ambient temperature

Particle Puff Characteristics

PDIA	Particle diameter of size class L
NPP	Number of particles per size class
TIPUF	Time sequence at which particles are released

Nuclear Burst Characteristics

YLD	Yield
HOB	Height of burst
GR	Ground range

Post-Blowoff Air Parameters

DZO	Initial spatial mesh description
ALPHA	Dimensionless dust layer absorption coefficient
ALBED	Dust layer albedo
CMIX	Turbulent conductivity coefficient

Integration Data

DT	Initial time step
EPS	Relative allowable integration error
TMAX	Maximum time for integration
MCYC	Maximum number of time cycles
DTLIM	Smallest allowable time step

Table 17. DUSLAR PROGRAM SIZE LIMITATIONS

$n_s \le 10$	Number of particle size classes
$n_m \le 50$	Number of meshpoints in air
$n_p \le 200$	Number of particle puffs $3\ n_s n_p + n_m \le 400$
$n_c \le 50$	Total number of conduction cells in soil and air (pre-blowoff conditions)

air inside the dust layer. It is obvious that other average dust layer heights and temperatures could be defined. However, in the absence of any data supporting other definitions, the one defined above has been incorporated in DUSLAR.

A set of calculations was performed for shot Priscilla which has a height of burst of 700 ft and yield of 36.6 kt. The flux and fluence histories normal to the ground surface at a ground range of 1800 ft as calculated by the model in DUSLAR are shown in Figure 20. Similar shapes can be generated for other yields, HOBs, and ground ranges. Results of a number of calculations are shown in Tables 18 and 19. The input data for the cases are based on the best available information or judgments without resorting to detailed parameter studies for finding optimum parameter values that would fit the data. In Table 18, the column titled "backed out °K" is taken as the "experimental" data against which the temperatures are to be compared. The procedure used to obtain these data has been discussed in the earlier sections of this report. The next column shows dust layer average temperatures computed as if no particles could melt. These temperatures are consistently too high. The last column shows the computed average temperatures when dust particle melting is allowed. In addition, only one particle size was assumed. The temperatures thus computed do not show the same functional behavior with respect to the ground range as compared to the backed-out values and the results from the case where particles are not allowed to melt. This may be explained to a significant degree by the use of one particle size class as opposed to the four that were used in the other problem. This has, however, not been confirmed. Table 19 shows predicted mean dust layer heights at the time of shock arrival for the same cases analyzed in Table 18. It may be quite surprising that the thicknesses obtained are relatively thin layers. It may be argued that these are not realistic since high temperatures were observed experimentally in several tests at tens of feet above the ground (Figure 20). These

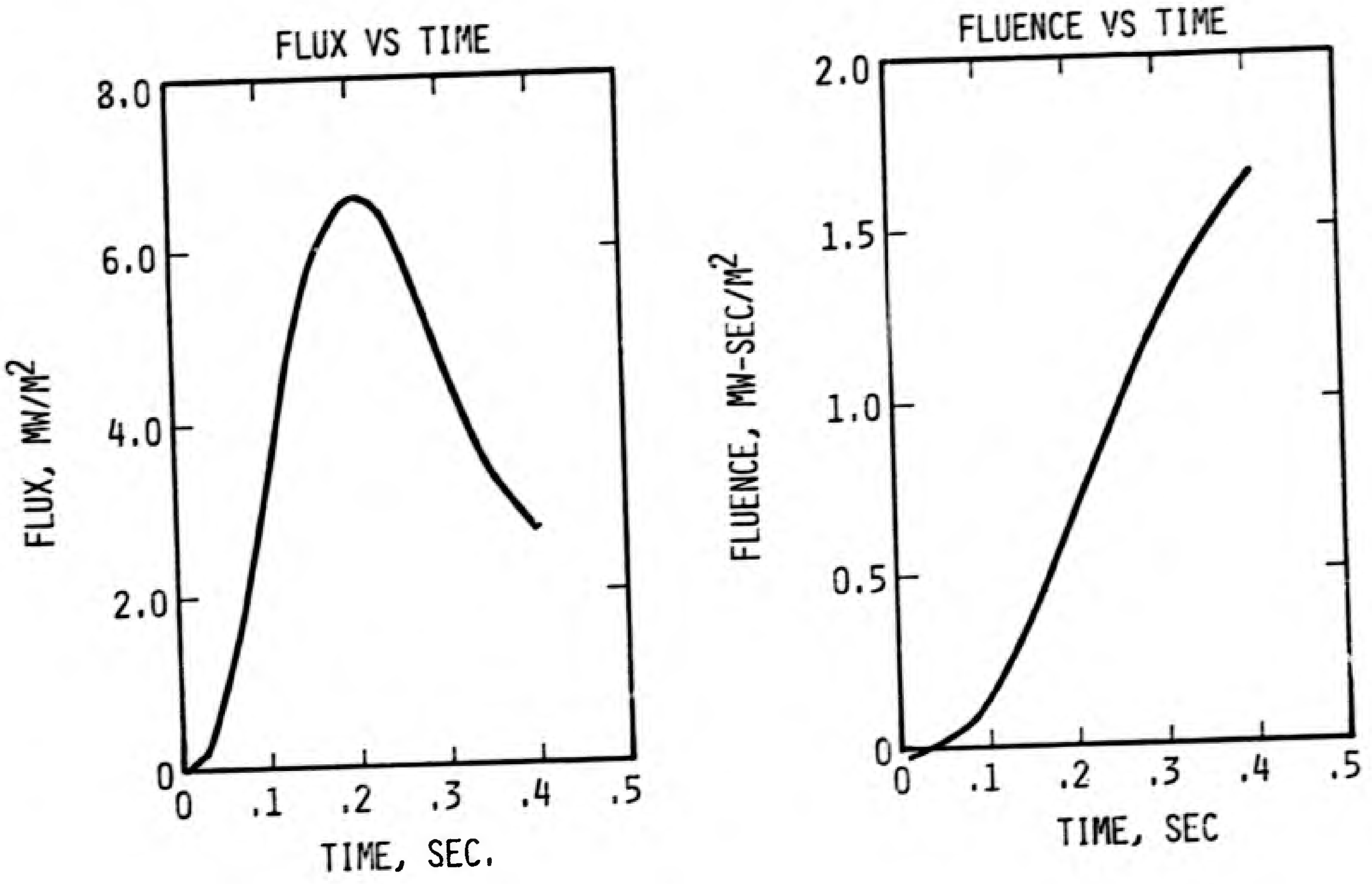

Figure 20. Flux and Fluence Histories Normal to the Ground Surface for Priscilla at 1800 ft.

Table 18. RESULTS FOR PRISCILLA (HOB = 700 ft, YLD = 36.6 KT)

RANGE		BACKED OUT °K	LAYER	
			THERMAL TEMPERATURE RISE*	
			DUSLAR WITHOUT MELTING PARTICLES	DUSLAR WITH MELTING PARTICLES
K FT	KM		°K	°K
1.05	0.320	2500	>4500	1370
1.35	0.412	1800	3300	1450
1.80	0.549	1300	1240	1520
2.50	0.762	250	500	860

* Only one particle size was considered for the cases where particles were allowed to melt, otherwise, four sizes were used.

Table 19. RESULTS FOR PRISCILLA (HOB = 700 ft, YLD = 36.6 KT)

RANGE K FT	DUSLAR THERMAL LAYER THICKNESS, M*	
	WITHOUT MELTING	WITH MELTING
1.05	NA	.052
1.35	0.19	.054
1.80	0.19	.058
2.50	0.19	.029

* Only one particle size was considered for the cases where particles were allowed to melt, otherwise, four sizes were used.

measurements, however, indicated only short bursts of high temperatures, possibly implying unstable temperature conditions near the ground surface. Hence the thin layers that are predicted may not be unreasonable.

Typical time histories of the dust layer height and the average dust layer temperature are shown in Figures 21 and 22. The curves in these figures terminate at the time of shock arrival. A typical dust layer air temperature profile is shown in Figure 23. This profile shows that most of the absorption of the thermal radiation occurs near the center of the layer. The curve also shows a deficiency in the present model near the ground surface. Thermal conduction from the ground into the air during the blowoff phase is presently not modeled. If it were, the temperature near the ground surface should be somewhere in the vicinity of 700 to 800°C. This effect is not expected to contribute significantly to the calculation of an average thermal layer temperature.

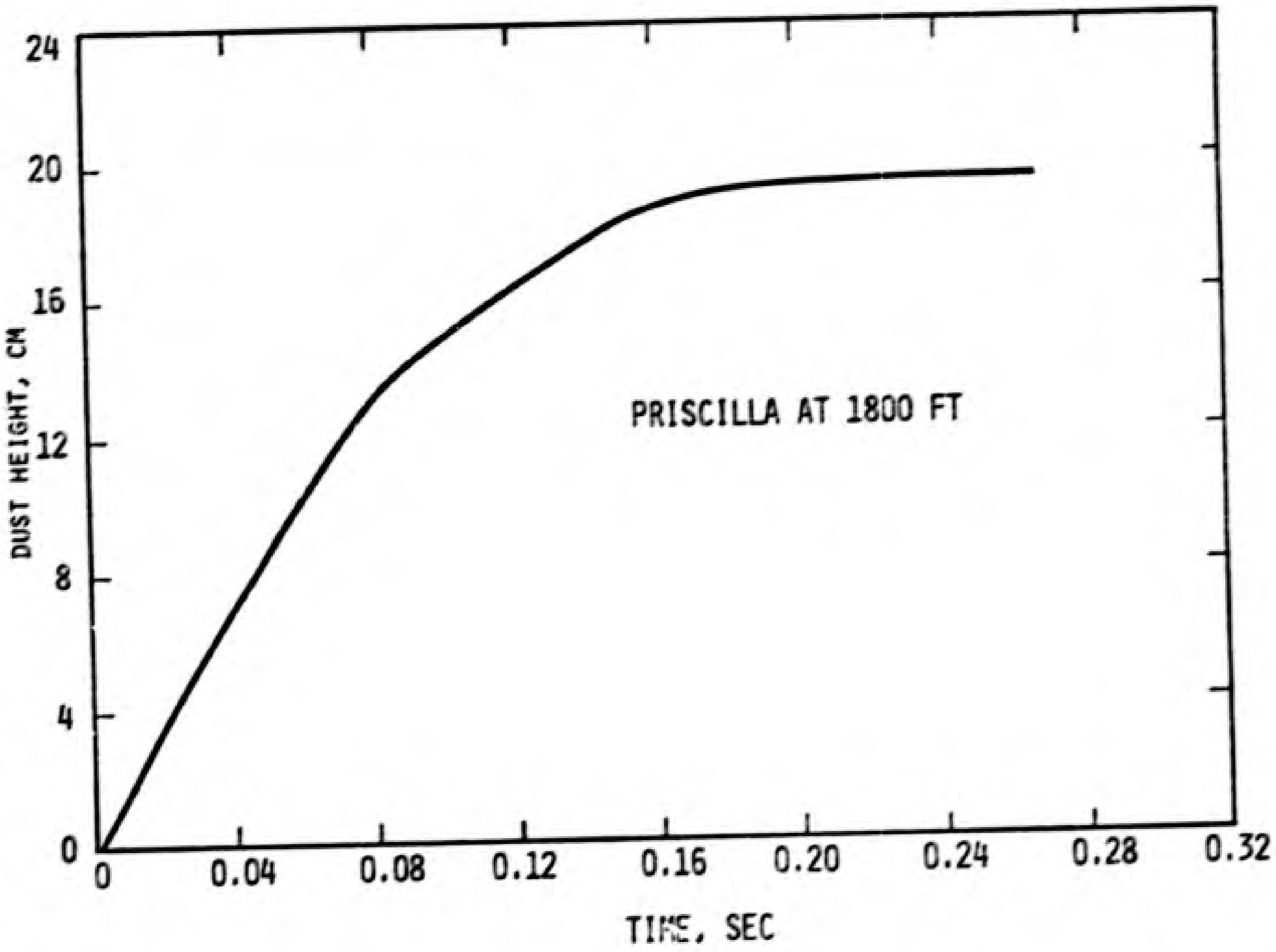

Figure 21. Dust Layer Evolution Calculated by DUSLAR

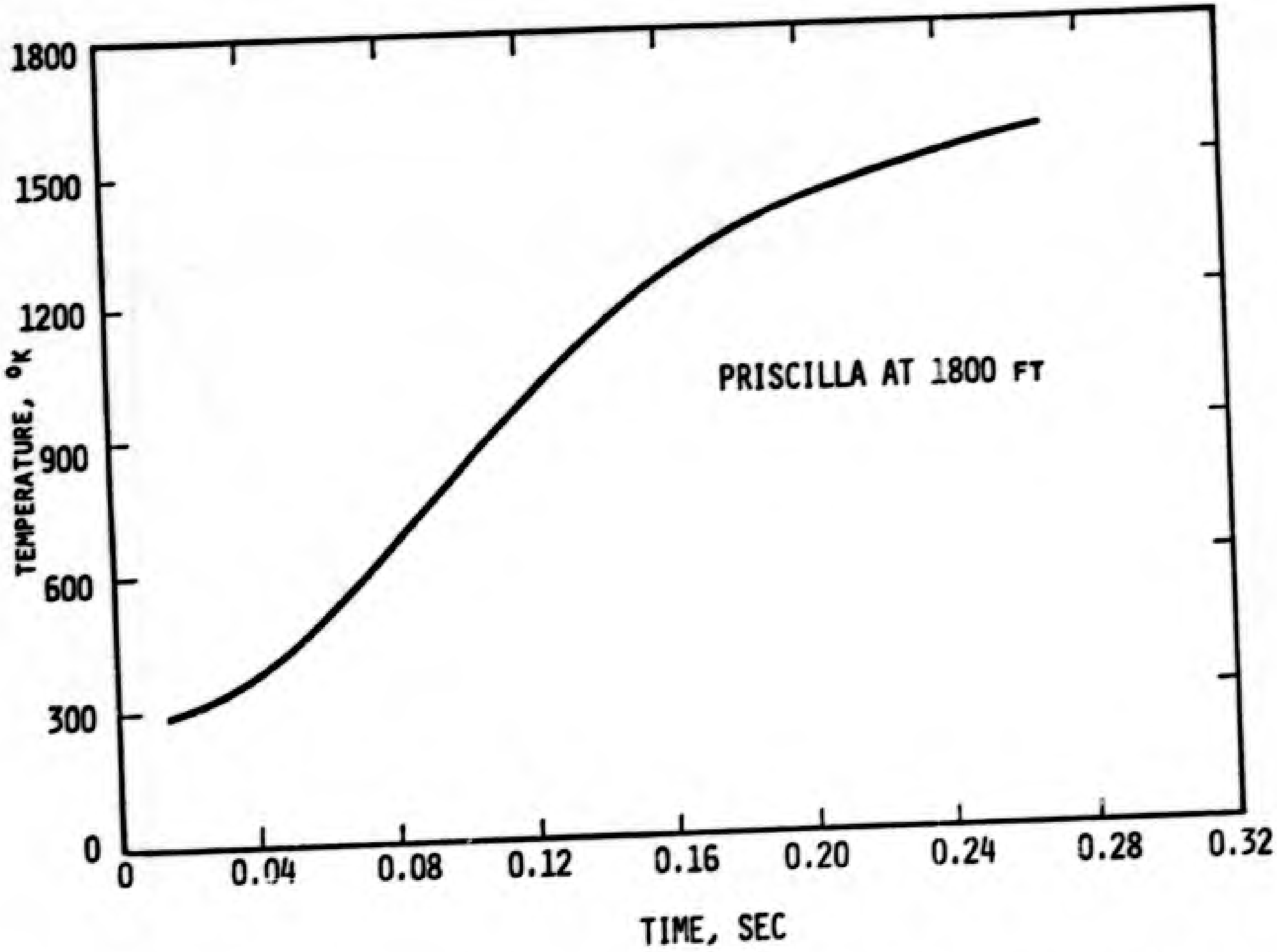

Figure 22. Dust Layer Mixed Mean Air Temperature as a Function of Time Calculated by DUSLAR

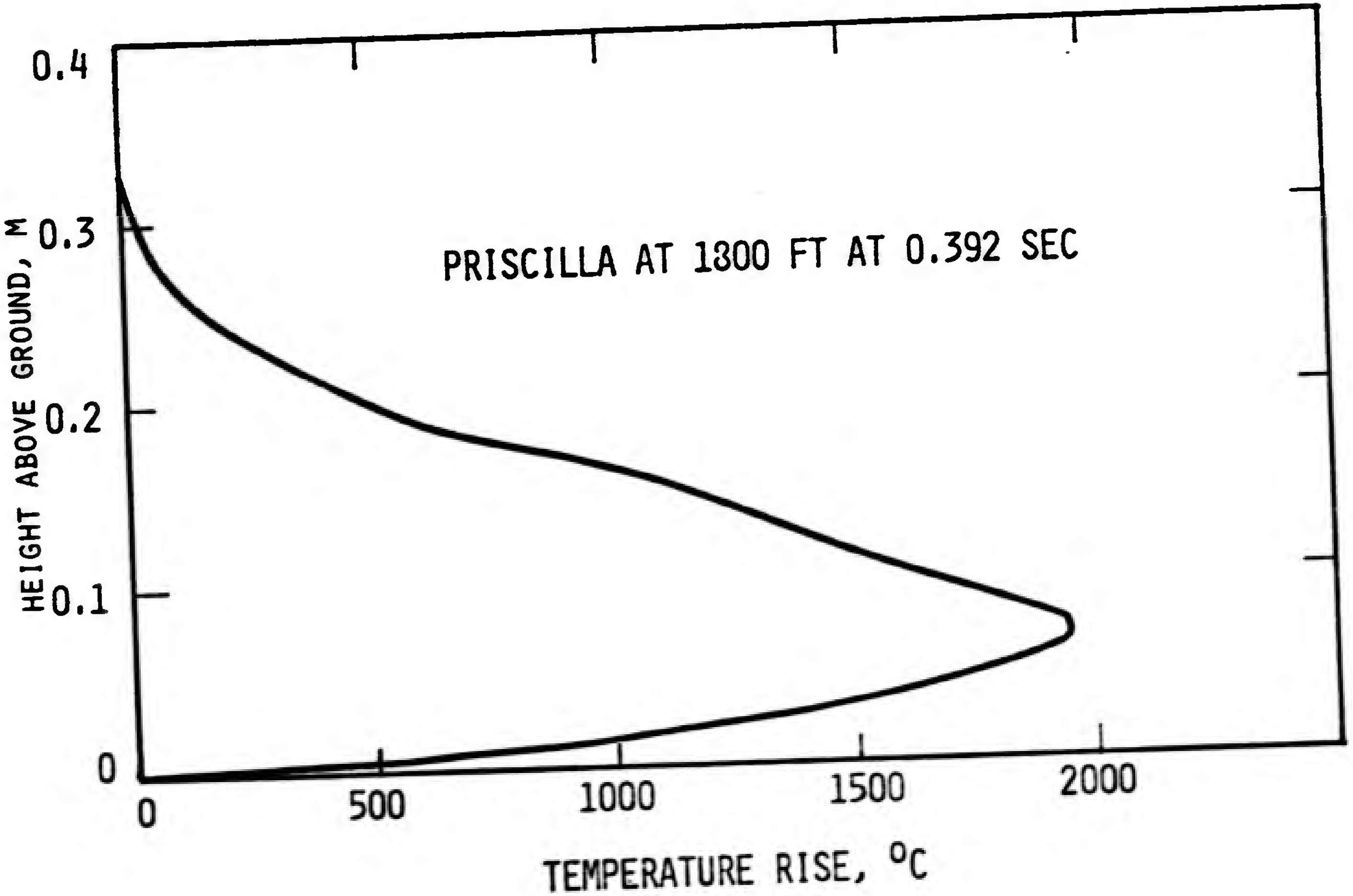

Figure 23. Air Temperature Profile in the Dust Layer

Section 5

SUPPORT FOR HULL CALCULATIONS

In addition to the work discussed above, SAI provided support to the DNA precursor program at the Air Force Weapons Laboratory (AFWL). This support was in three areas: (1) maintenance and improvement of the HULL code system, (2) supporting the calculational and analysis activities related to the DNA precursor program, and (3) performing, analyzing and modeling AFWL thermal layer calculations.

The first of these areas involved, by far, the bulk of the effort. The HULL code system was maintained in an operational state throughout almost all of the contract period. Down time was attributable to extensive software implementations at the AFWL Computer Center. In addition, the entire HULL system and its auxilliary routines were converted to usage on the CDC 7600. All coding modifications were appropriately documented on the HULL Executive Language file. Modifications were made to HULL in addition to the original implementation, since significant software modifications were made at AFWL beyond those originally expected. Furthermore PULL, the graphics package in HULL, was modified to allow use of the FR80, delivered at the AFWL early in 1976. The FR80 is a sophisticated hardware device for producing fine resolution plots or printing on either microfiche or 16mm film.

The effort expended in supporting the calculational and analysis activities consisted primarily of solving operational problems as they occurred, and assessing the correctness of any coding modification made by the AFWL. Modifications to HULL that were made as a result of this effort were documented in the HULL Executive Language file.

Finally, the effort expended in the third area (i.e., performing, analyzing and modeling AFWL thermal layer calculations) consisted of two principal investigations. The first was a sensitivity analysis of the AFWL thermal predictor to changes in both zoning and physical input parameters. The second was the calculation and modeling of 10 kt burst detonating at 500 feet. The reporting documentation developed as a result of these tasks will be documented as AFWL reports.

Section 6

CONCLUSIONS AND RECOMMENDATIONS

6.1 CONCLUSIONS

The results of two aspects of precursor waves have been analyzed and presented in this report. First procedures to determine the thermal layer temperature from experimentally observed overpressures from NTS atmosphere shots have been reviewed and data reanalyzed. "Backed out" temperatures calculated in this way were found to be reasonable when compared with dust velocity models and the thermal layer model developed in this report.

Second a model has been formulated that can describe the physical behavior of the ground surface and the near-ground layer when subjected to intense nuclear thermal radiation. This model, named DUSLAR, is based, in part, on experimental data available from solar furnace tests and new analyses of NTS-type soils.

Early results with the model show that it may be used as a predictive technique for evaluating pre-shock thermal layer temperatures. Insufficient parameter studies have been conducted to truly evaluate its limitations. Since the model is a mixture of theory and empiricism, there are several parameters that could probably be optimized. Lack of time has prevented doing this. These parameters were chosen on a best-estimate basis. Comparison against experimental data has also been limited. Direct comparison against experimental data has, so far, not been possible because the reliability of the limited data that are available is questionable. However, comparing the calculations with reduced temperatures, as has been done in Section 4, appears feasible. Further analyses along these lines would be beneficial.

6.2 RECOMMENDATIONS

A number of improvements are possible to increase the capability of DUSLAR or to make it computationally more efficient. DUSLAR was developed primarily to understand the physics of the blowoff process. Therefore, the integration routine, described in Section 3.12, was used because it was readily available and proven for problems of the present nature. More efficient schemes exist, however, and their applicability should be tested. A more efficient integration routine and an improved procedure for writing the results onto a file that can be saved will improve the efficiency of the code.

The physical description of the process can be improved in several ways. The code is presently limited to particles that can melt but that cannot evaporate. Calculational procedures can be extended to include evaporation, but this will increase the computation time because of the additional equations that have to be solved. These equations involve the description of the particle radius reduction and the effect of the vaporized material on the air thermodynamic properties.

The DUSLAR model computes conduction into the soil only until initiation of blowoff. A more accurate description of the temperature field in the soil, and hence the initial temperature of the particles that are ejected into the air, requires a conduction solution with one moving boundary. Although simple to implement, the conduction model itself does require some development. The thermodynamic property correlations for air, as incorporated in DUSLAR, are reasonably accurate for moderate temperature rises (up to 1000°K). Beyond this, increasing errors are introduced. More accurate relationships are a first requirement to extending the present model.

In DUSLAR, the motion of dust particles is represented in the form of a series of puffs for which the motion of the center of mass is computed continuously. When a puff crosses a mesh boundary, the particles are distributed uniformly within the particular mesh in order to compute the radiation attenuation through the dust layer. As expected, this procedure is somewhat sensitive to the mesh size description. An alternative puff description, one which has a finite width, should eliminate this sensitivity to a great extent. It requires, however, a more elaborate bookkeeping procedure and, hence, increased computation. Several other improvements are possible, all of which have to do with definitions of average temperature. These are considered to have only minor effects on the results.

It may be concluded that DUSLAR shows promise as a tool for predicting thermal layer temperatures. Considerable work still remains before it could be used on a routine basis. However, in its present form, it can be used for preliminary analysis of those soils for which the basic blowoff characteristics have been evaluated experimentally.

REFERENCES

1. R. T. Liner, J. T. Powers, J. A. Shannon and P. L. Versteegan, "Nuclear Precursor Phenomenology and Sweep-Up Dust Cloud Model Development," DNA 3781F.

2. J. T. Powers, J. E. Mansfield, R. T. Liner, "Precursor Sweep-Up Dust Cloud Model and Thermal Layer Model Development," DNA 3876F.

3. T. M. Knasel, et al., "Experimental Studies of Soil Thermal Irradiation", SAI-78-540-WA, in publication. Also "A Review of Non-Ideal Blast Wave Physics," a briefing presented 24 Aug 1976.

4. P. J. Dolan, "Capabilities of Nuclear Weapons, Part I," DNA EM-1.

5. P. A. Ellis, et al., "Nuclear Weapons Blast Phenomena, Vol. I," DASA 1200-1.

6. B. S. Chambers, III, Progress Reports 9 and 10, "Definition of Precursed Waveforms for Nuclear Air Shock," AFWL report, January 31, 1975.

7. J. W. Kirsch, et al., "The Near-Surface Nuclear Dust Cloud," DNA 3962F, April 1976.

8. D. C. Sachs, L. M. Swift, and F. M. Sauer, "Report to the Test Director, Operation Teapot, Project 1.10, Airblast Overpressure and Dynamic Pressure over Various Surfaces," WT-1109.

9. L. M. Swift, D. C. Sachs, and A. R. Kriebel, "Operation Plumbob, Project 1.3, Air Blast Phenomena in the High Pressure Region," WT-1403.

10. T. M. Knasel, "Thermal Induced Blowoff: A Report on Experimental Studies, Vol. 1," DNA-3723F-1, April 1975.

11. R. W. Grimshaw, "The Chemistry and Physics of Clays and Other Ceramic Materials," Wiley-Interscience, 1971.

REFERENCES (Cont'd)

12. R. Liner, "Pre-Shock Thermal Layer Formation and Dust Lofting by Nuclear Bursts," Science Applications, Inc., SAI-73-549-AR, 1973.

13. R. Liner, J. T. Powers, J. A. Shannon, P. L. Versteegen, "Nuclear Precursor Phenomenology and Sweep-up Dust Cloud Model Development," DNA-3781F (SAI-74-627-WA), 1975.

14. S. L. Soo, Fluid Dynamics of Multiphase Systems, Blaisdell Publishing Company, 1967.

15. R. D. Cadle, Particle Size, Theory and Application, Reinhold Publishing Company, 1965.

16. L. B. Torobin and W. H. Gauvin, "Fundamental Aspects of Solids-Gas Flow, Part I: Introductory Concepts and Idealized Sphere Motion in Viscous Regime," The Canadian Journal of Chemical Engineering, 37, pp. 129-141, August 1959.

17. S. Goldstein, Editor, Modern Developments in Fluid Mechanics, Vol. 1 and 2, Dover Publications, Inc., 1965.

18. W. M. Rohsenow, and T. P. Hartnett, editors, Handbook of Heat Transfer, McGraw Hill, 1973.

19. Bird, R. B., W. E. Stewart, E. N. Lightfoot, Transport Phenomena, John Wiley & Sons, Inc., 1960.

20. A. S. Chenoy, J. R. Williams, J. D. Clement, "Measurements of the Extinction Parameters of Hot Seeded Hydrogen at 1 Atmosphere Pressure," NASA CR-1504, February 1970.

21. F. Kreith, Principles of Heat Transfer, International Textbook Company, 1958.

REFERENCES (Cont'd)

22. R. E. Funderlic, editor, The Programmers' Handbook, K-1729, February 1968.

Appendix A

SOLUTION PROCEDURE FOR SIMULTANEOUS LINEAR EQUATIONS

The set of N linear equations defined by the recurrence relationship

$$a_i x_{i-1} + b_i x_i + c_i x_{i+1} = d_i \qquad i = 1, 2, \ldots N$$

where

$$a_1 = c_N = 0$$

can be written in matrix form as:

$$\begin{bmatrix} b_1 & c_1 & & & \\ a_2 & b_2 & c_2 & & \\ & a_3 & b_3 & c_3 & \\ & & & \vdots & \\ & & & a_N & b_N \end{bmatrix} \begin{bmatrix} x_1 \\ x_2 \\ x_3 \\ \vdots \\ x_N \end{bmatrix} = \begin{bmatrix} d_1 \\ d_2 \\ d_3 \\ \vdots \\ d_N \end{bmatrix}$$

The tridiagonal form of the coefficient matrix allows for a very efficient solution algorithm. This method is a simplification of the Gauss elminination procedure and goes as follows: Assume that the solution to the above system can be written in the following form

$$x_K = e_K x_{K+1} + f_K.$$

Substituting this solution in the original set of equations involving the known constants a_i, b_i, c_i, d_i gives

$$a_K \left[e_{K-1} x_K + f_{K-1} \right] + b_K x_K + c_K x_{K+1} = d_K .$$

Solving this equation for x_K gives

$$x_K = \frac{c_K x_{K+1} + d_K - a_K f_{K-1}}{a_K e_{K-1} + b_K} .$$

Comparing this equation with the assumed solution gives

$$e_K = \frac{- c_K}{a_K e_{K-1} + b_K}$$

$$f_K = \frac{d_K - a_K f_{K-1}}{a_K e_{K-1} + b_K} .$$

These two expressions for e_K and f_K define recurrence relations for these coefficients. If e_1 and f_1 are known, then all e's and f's can be calculated. Since $a_1 = 0$, it follows that

$$e_1 = \frac{- c_1}{b_1} ; \qquad f_1 = \frac{d_1}{b_1} .$$

Thus, all e's and f's are known. When one value of x is known, all others can be determined from the assumed solution. The known value for x is x_N, since $e_N = 0$ (from $c_N = 0$). Working backwards, all other values of x can then be found.

DISTRIBUTION LIST

DEPARTMENT OF DEFENSE

Asst. to the Secretary of Defense
Atomic Energy
ATTN: Honorable Donald R. Cotter

Director
Defense Advanced Rsch. Proj. Agency
ATTN: NMRO
ATTN: PMO
ATTN: STO
ATTN: Tech. Lib.

Director
Defense Civil Preparedness Agency
ATTN: Admin. Officer

Defense Documentation Center
Cameron Station
12 cy ATTN: TC

Director
Defense Intelligence Agency
ATTN: DT-1C
ATTN: DT-2, Wpns. & Sys. Div.
ATTN: DB-4C, Edward O'Farrell

Director
Defense Nuclear Agency
ATTN: TISI, Archives
ATTN: DDST
2 cy ATTN: SPSS
3 cy ATTN: TITL, Tech. Lib.

Chairman
Dept. of Defense Explo. Safety Board
ATTN: DD/S&SS
ATTN: Thomas Zaker

Commander
Field Command, Defense Nuclear Agency
ATTN: FCT
ATTN: FCTMOF
ATTN: FCPR

Chief
Livermore Div., Fld. Command, DNA
Lawrence Livermore Laboratory
ATTN: FCPRL

Chief
Test Construction Division
Field Command, Test Directorate
ATTN: FCTC

Under Secy. of Def. for Rsch. & Engrg.
ATTN: S&SS(OS)

DEPARTMENT OF THE ARMY

Dep. Chief of Staff for Rsch. Dev. & Acq.
ATTN: Tech. Lib.

DEPARTMENT OF THE ARMY (Continued)

Chief of Engineers
ATTN: DAEN-RDM
ATTN: DAEN-MCE-D

Deputy Chief of Staff for Ops. & Plans
ATTN: Tech. Lib.

Commander
Harry Diamond Laboratories
ATTN: DRXDO-TI, Tech. Lib.
ATTN: DELHD-NP

Commander
Redstone Scientific Information Ctr.
U.S. Army Missile Command
ATTN: Chief, Documents

Director
U.S. Army Ballistic Research Labs.
ATTN: DRDAR-BLE, W. Taylor
ATTN: Tech. Lib., Edward Baicy
ATTN: DRDAR-BLE, J. H. Keefer
ATTN: DRXBR-X, Julius J. Meszaros

Director
U.S. Army Engr. Waterways Exper. Sta.
ATTN: William Flathau
ATTN: Tech. Lib.
ATTN: Guy Jackson
ATTN: John N. Strange

Commander
U.S. Army Mat. & Mechanics Rsch. Ctr.
ATTN: Tech. Lib.

Commander
U.S. Army Materiel Dev. & Readiness Cmd.
ATTN: Tech. Lib.

Commander
U.S. Army Mobility Equip. R&D Ctr.
ATTN: Tech. Lib.

Commander
U.S. Army Nuclear Agency
ATTN: Tech. Lib.

DEPARTMENT OF THE NAVY

Chief of Naval Material
ATTN: MAT 0323

Chief of Naval Operations
ATTN: OP 03EG
ATTN: OP 981

Chief of Naval Research
ATTN: Nicholas Perrone
ATTN: Code 464, Thomas P. Quinn
ATTN: Tech. Lib.
ATTN: Code 464, Jacob L. Warner

DEPARTMENT OF THE NAVY (Continued)

Officer-in-Charge
Civil Engineering Laboratory
ATTN: R. J. Odello
ATTN: Tech. Lib.

Commander
David W. Taylor Naval Ship R&D Ctr.
ATTN: Code L42-3, Library

Commander
Naval Electronic Systems Command
Naval Electronic Systems Cmd. Hqs.
ATTN: PME 117-21A

Commander
Naval Facilities Engineering Cmd. Hqs.
ATTN: Tech. Lib.
ATTN: Code 03A
ATTN: Code 04B

Director
Naval Research Laboratory
ATTN: Code 2600, Tech. Lib.

Commander
Naval Sea Systems Command
ATTN: Code 03511
ATTN: ORD-91313, Lib.

Commander
Naval Ship Engineering Center
ATTN: Tech. Lib.
ATTN: NSEC 6105G

Commander
Naval Ship Rsch. & Dev. Ctr.
Underwater Explosive Research Division
ATTN: John Gordon
ATTN: Tech. Lib.

Officer-in-Charge
Naval Surface Weapons Center
ATTN: Code WA501, Navy Nuc. Prgms. Off.

Commander
Naval Surface Weapons Center
ATTN: Tech. Lib.

Director
Strategic Systems Project Office
ATTN: NSP-272
ATTN: NSP-43, Tech. Lib.

DEPARTMENT OF THE AIR FORCE

AF Geophysics Laboratory, AFSC
ATTN: LWW, K. C. Thompson

AF Institute of Technology, AU
ATTN: Lib., AFIT Bldg. 640, Area B

AF Weapons Laboratory, AFSC
ATTN: DEX
ATTN: DES-S, Maj Ganong
ATTN: DES-C, Charles Needham
ATTN: SUL

DEPARTMENT OF THE AIR FORCE (Continued)

Headquarters
Air Force Systems Command
ATTN: DLCAW

Hq. USAF/IN
ATTN: INATA

Hq. USAF/RD
ATTN: RDQSM

Commander in Chief
Strategic Air Command
ATTN: NRI-STINFO, Library

DEPARTMENT OF ENERGY

Department of Energy
Albuquerque Operations Office
ATTN: Doc. Con. for Tech. Lib.

Department of Energy
Division of Headquarters Services
ATTN: Doc. Con. for Class. Tech. Lib.

Department of Energy
Nevada Operations Office
ATTN: Doc. Con. for Tech. Lib.

Division of Military Application
ATTN: Doc. Con. for Test Office

University of California
Lawrence Livermore Laboratory
ATTN: Larry W. Woodruff, L-96
ATTN: Tech. Info. Dept L-3

Los Alamos Scientific Laboratory
ATTN: Doc. Con. for Reports Lib.

Sandia Laboratories
ATTN: Doc. Con. for Tech. Lib.

Sandia Laboratories
ATTN: Doc. Con. for Org 3422-1, Sandia Rpt. Coll.

DEPARTMENT OF DEFENSE CONTRACTORS

Aerospace Corporation
ATTN: Tech. Info. Services

The Boeing Company
ATTN: Aerospace Library

Civil/Nuclear Systems Corp.
ATTN: Robert Crawford

EG&G, Inc.
Albuquerque Division
ATTN: Tech. Lib.

General Electric Company
TEMPO-Center for Advanced Studies
ATTN: DASIAC

DEPARTMENT OF DEFENSE CONTRACTORS (Continued)

IIT Research Institute
ATTN: Tech. Lib.

Institute for Defense Analyses
ATTN: IDA Librarian, Ruth S. Smith

Kaman Sciences Corporation
ATTN: Library

Lockheed Missiles & Space Co., Inc.
ATTN: Tech. Lib.

Lovelace Foundation for Medical Education & Rsch.
ATTN: Tech. Lib.

Physics International Company
ATTN: Doc. Con. for E. T. Moore
ATTN: Doc. Con. for Coye Vincent
ATTN: Doc. Con. for Tech. Lib.

R&D Associates
ATTN: Robert Port
ATTN: J. G. Lewis
ATTN: Tech. Lib.

Science Applications, Inc.
ATTN: Tech. Lib.

Science Applications, Inc.
ATTN: R. A. Shunk

Science Applications, Inc.
ATTN: T. M. Knasel
ATTN: P. L. Versteegan
ATTN: J. A. Powers

DEPARTMENT OF DEFENSE CONTRACTORS (Continued)

Southwest Research Institute
ATTN: Wilfred E. Baker
ATTN: A. B. Wenzel

SRI International
ATTN: Burt R. Gasten
ATTN: George R. Abrahamson

Systems, Science and Software, Inc.
ATTN: Donald R. Grine
ATTN: Tech. Lib.

TRW Defense & Space Sys. Group
ATTN: Tech. Info. Center, S-1930
ATTN: D. H. Baer, R1-2136
2 cy ATTN: Peter K. Dai, R1-2170

TRW Defense & Space Sys. Group
ATTN: E. Y. Wong, 527/712
ATTN: Gregg Hulcher

The Eric H. Wang Civil Engineering Rsch. Fac.
ATTN: Larry Bickle
ATTN: Neal Baum

Weidlinger Assoc. Consulting Engineers
ATTN: Melvin L. Baron

Weidlinger Assoc. Consulting Engineers
ATTN: J. Isenberg